Development of Terahertz Quantum Well Photodetector at 3 THz

by

Yue Zhuo

A thesis

presented to the University of Waterloo

in fulfilment of the

thesis requirement for the degree of

Master of Applied Science

in

Electrical and Computer Engineering

Waterloo, Ontario, Canada, 2019

Author's Declaration

I hereby declare that I am the sole author of this thesis. This is a true copy of the thesis, including any required final revisions, as accepted by my examiners.

I understand that my thesis may be made electronically available to the public.

Abstract

This thesis reports a new terahertz ($f = 3.22$ THz) quantum well photodetector (THz QWP) as well as comprehensive numerical models simulating device active region and different grating couplers including traditional diffraction metal grating and novel patch antenna structure.

Among all the terahertz detectors, terahertz quantum well photodetector (THz QWP), has proved its fast optical response speed and remarkable sensitivity and shown great potential for applications in security, bio-medical technology and space communication. However, due to high requirements in experiment condition and growth quality, THz QWPs absorbed at 3 THz or lower have not been much developed yet. Furthermore, THz QWP working around 3 THz can be combined with one of the strongest terahertz emitters, terahertz quantum cascade laser (THz QCL), for ultrafast spectroscopy and imaging applications. Recently, THz QWPs integrated with different grating couplers have been explored and are now intensively investigated to improve device temperature performance.

In that regard, we aim to improve the simulation model and develop a new THz QWP absorbing at 3 THz. Moreover, numerical COMSOL models are built to analyze optical properties of traditional diffraction metal grating coupler and novel patch antenna coupler in this work. According to measured current density-voltage (j-V) profiles and absorption spectrum, the proposed THz QWP with a new active region design has its background-limited infrared performance (BLIP) temperature at 10 K and manages to achieve terahertz range absorption at

lower frequency around 3 THz. Results show a peak responsivity of 1.9 A/W, a peak detectivity of 4.63×10^{10} cmHz$^{1/2}$/W and an absorption range from 94.5 cm^{-1} (2.83 THz) to 142.7 cm^{-1} (4.25 THz). To our knowledge, this THz QWP has the lowest peak absorption frequency (3.22 THz) and it is the second one that works near 3 THz. Measured j-V profiles show a size-dependent shifting, indicating the existence of sidewall leakage currents, and the comparison between simulation and measurement results of j-V profiles reveals the consistency, especially at higher temperature. In addition, simulation results on 1D metal grating coupler and patch antenna coupler are demonstrated and they strongly agree with the experiment data from literatures as well as general rules of thumb.

Acknowledgements

I would like to thank my supervisor Prof. Dayan Ban for his patience and encouragement throughout my Master studies. This work would not have been possible without his support and guidance.

I want to express my gratitude to the readers of this thesis, Prof. Irene Goldthorpe and Prof. Youngki Yoon.

My deepest gratitude goes to Dr. Chao Xu, Dr. Shazzad Rassel and Dr. HoSung Kim for sharing their research experience with me.

I would like to thank my colleague, Dr. Chao Xu, for his tremendous effort in device fabrication and his involvement in device testing. I also want to express my thanks to my colleague Siyi Wang and Dr. Guocheng (Eric) Liu for their help in fabrication process.

I want express my thanks to Prof. Zbig Wasilewski, Alan Tam, Chris Deimert, Dr. HoSung Kim and all the growers involved for offering the opportunity to have my sample grown.

I would also like to thank Steven Zhang and Zhenwen Wang for providing technical help.

This work would not have been finished without the help and support of my colleagues. I would like to express my gratitude to Chao, Boyu, Xiaoliang, Jian, Siyi, Jacky, Alam, Asif, Cathy, Burak and Teppei for their company and interesting discussions during my Master studies. It is my pleasure to work with them and I really enjoy it.

I want to especially thank Boyu Wen, Prof. Chunlei Wang and Prof. Shuhong Xu for offering me their places to stay overnight in Waterloo in the last two terms.

Finally, I must express my very profound gratitude my to parents, for all the mental and financial support throughout all those years, and to my beloved wife, Mingyu Liu. I cannot write how much I thank her for everything. This accomplishment would not have been possible without the support from my family. Thank you.

Dedication

To my beloved wife, Mingyu,

And

To my parents.

Table of Contents

Table of Contents ..... **viii**

List of Tables ..... **xi**

List of Figures ..... **xii**

Chapter 1 Introduction **1**

1.1 Background and Motivation **1**

1.2 Literature Review **3**

1.2.1 Terahertz Radiation Applications 4

1.2.2 Terahertz Detectors 5

1.2.3 Quantum Well Infrared Photodetectors 7

1.2.4 Terahertz Quantum Well Photodetectors 12

1.3 Research Objectives **14**

1.4 Thesis Overview **15**

Chapter 2 Terahertz Quantum Well Photodetector **17**

2.1 Active Region Model **17**

2.1.1 Quantum Well Heterostructures 18

2.1.2 Intersubband Transition 21

2.1.3 Many-body Effect 23

2.2 Photoconductive THz QWP 25

2.2.1 Optimum Electronic Confinement 25

2.2.2 Photocurrent Transport 27

2.2.3 Responsivity 31

2.2.4 Detectivity 32

2.2.5 Light Coupling Geometries 34

2.3 Device Simulation 35

2.3.1 Potential Calculation 36

2.3.2 Absorption Spectrum Simulation 37

2.3.3 Dark Current Simulation 40

2.4 Electric Characterization 42

2.4.1 j-V Characteristics and BLIP temperature 44

2.4.2 Absorption Spectrum 52

2.4.3 Responsivity 54

2.4.4 Detectivity 59

2.5 Conclusion 61

Chapter 3 Light Couplers for THz QWP 62

3.1 Metal Grating Coupler 62

3.1.1 Metal Grating Coupler Structure and Mechanism 63

3.1.2 Metal Grating Coupler Key parameters 64

3.1.3 Simulation Results 65

3.2 Patch Antenna 69

3.2.1 Patch Antenna Mechanism 70

3.2.2 Patch Antenna THz QWP Key parameters 71

3.2.3 Simulation Results 74

3.3 Conclusion **77**

Chapter 4 Conclusion and Future Work **78**

References **82**

Appendices **89**

List of Tables

Table 2.1 Structure parameters of A0175 [44], V266 and V267 [54] 38

Table 2.2 Simulated parameters used to calculate detectivity of G0219 60

Table 3.1 Detail settings of the COMSOL model..... 66

Table A.1 Growth layer structure of G0219 90

Table B.1 Fabrication processing sheet 94

List of Figures

Figure 1.1 Electromagnetic spectrum 2

Figure 1.2 Schematic of bolometer 6

Figure 1.3 Schematic of photomixing 7

Figure 1.4 Schematic of single module in QWIP, showing the electron capture and excitation processes 9

Figure 1.5 Energy band diagram of photovoltaic QWIP with (a) graded collector; (b) square collector 10

Figure 1.6 Energy band diagram of (a) photovoltaic QWIP with four-zone scheme, 1: capture zone, 2: tunneling zone, 3: emission zone, 4, drift zone; (b) QCD 11

Figure 1.7 Schematic of THz QWP with 45° facet 13

Figure 2.1 Schematic of quantum well heterostructure, E_0: ground energy state, E_1: first excited energy state 19

Figure 2.2 Schematic of Intersubband transition selection rule, only the component of the electric field of incident light that is parallel to growth direction can be absorbed by active region [43] 21

Figure 2.3 (a) bound-to-continuum (b) bound-to-bound intersubband transition..... 26
Figure 2.4 bound-to-quasibound intersubband transition 27
Figure 2.5 Schematic diagram of carrier transportation in THz QWP, j: total current; j_c: captured current; j_e: emission current; p_c: capture probability 28
Figure 2.6 Schematic diagram of dark current components, there are three portions of dark current in THz QWP: 1 tunneling; 2 thermionic emission; 3, thermal-assisted tunneling ... 30
Figure 2.7 Simulated (using developed MATLAB model) conduction band and confined energy levels in THz QWP (V266, structure parameters extracted from [54], see Table 2.1)..... 37
Figure 2.8 Simulation (calculated using developed MATLAB model) and experiment results(extracted from [44]) of absorption spectrum (A0175) including many body effects; inset: simulated band diagram and wavefunctions of A0175 38
Figure 2.9 Simulation (calculated using developed MATLAB model) and experiment results (extracted from [54]) of absorption spectrum (V266) including many body effects; inset: simulated band diagram and wavefunctions of V266..... 39
Figure 2.10 Simulation (calculated using developed MATLAB model) and experiment results (extracted from [54]) of absorption spectrum (V267) including many body effects; inset: simulated band diagram and wavefunctions of V267..... 39
Figure 2.11 Extract drift mobilities as a function of temperature from [50] 41
Figure 2.12 Simulation (calculated using developed MATLAB model) and experiment results (extracted from [50]) of dark current (V267) based on transmission coefficient model; inset: simulated band diagram and wavefunctions of V267..... 41

Figure 2.13 Simulation (calculated using developed MATLAB model) and experiment results (extracted from [55]) of dark current (L924) based on transmission coefficient model; inset: simulated band diagram and wavefunctions of L924 42
Figure 2.14 Top view of the device mounted on a package (squares in dark gold color are the top contacts for different device mesas; and surrounding gold is the common bottom contact). Inset: sideview of the device and package showing the 45 degree facet 44
Figure 2.15 Experiment setup of IV characterization 45
Figure 2.16 Measured dark current density of G0219 (device size: 600 μm) from 8 K to 16 K.. 46
Figure 2.17 Measured background current density of G0219 (device size: 600 μm) from 9 K to 16 K..... 46
Figure 2.18 Ratio between background and dark current density as a function of bias voltage of G0219 (device size: 600 μm) from 9 K to 16 K 47
Figure 2.19 Ratio between background and dark current density as a function of temperature (device size: 600 μm). Calculated BLIP temperature of G0219 is 10 K 47
Figure 2.20 Comparison between simulation and measured dark current density as a function of bias for G0219 (device size: 600 μm)..... 49
Figure 2.21 Current density as a function of bias voltage of G0219 (device size: 600 μm). Barrier breakdown observed under ±32 mV at 8, 9 and 10 K 50
Figure 2.22 Measured dark current density as a function of bias for devices with different mesa sizes at (a) 9 K, (b) 10 K and (c) 12 K 51
Figure 2.23 Experiment setup of spectrum measurement..... 53
Figure 2.24 Normalized spectrum of G0219 (device size: 600 μm) measured under 25 mV at 7.7 K. Peak response at 107.32 cm^{-1} 54

Figure 2.25 Experiment setup of responsivity characterization 55
Figure 2.26 Calculated photocurrent of G0219 (device size: 600 μm) from 9 K to 12 K as a function of bias voltage under 1173 K blackbody radiation 56
Figure 2.27 Spectral power density for different cases 58
Figure 2.28 Calculated responsivity of G0219 (device size: 600 μm) from 9 K to 12 K 59
Figure 2.29 Calculated detectivity of G0219 (device size: 600 μm) from 9 K to 12 K 60
Figure 3.1 Schematic of metal grating coupler in QWIP, L: grating period, h: grating height and F: filling factor 63
Figure 3.2 Schematic of numerical model geometry, light comes from the bottom side of substrate and is reflected and diffracted by metal grating structure on the top contact 65
Figure 3.3 Simulation result on electric field pattern at different wavelength: (a) 6 μm, (b) 5 μm, and (c) 3.75 μm (L = 1.5 μm, h = 0.3 μm, F = 60%). x, y axes are in μm 67
Figure 3.4 Simulation results of coupling efficiency with different (a) period (L), (b) height (h) and (c) filling factor (F) 68
Figure 3.5 Schematic of patch antenna structure in QWIP, d is the size of waveguide cavity 70
Figure 3.6 Top view of patch antenna structure and schematic of how patch antenna works [39] 72
Figure 3.7 Electric field distribution pattern of patch antenna coupling structure 75
Figure 3.8 Calculated reflection of patch antenna structure compared with measurement result from [39] 76
Figure C.1 Schematic of packaging process 95

Chapter 1 Introduction

1.1 Background and Motivation

Terahertz (THz) science and technology, ranging from 1 THz to 10 THz in frequency, has attracted significant interests and witnessed remarkable development in the past decades. Due to its wide range of potential applications, especially in biomedicine, high-speed telecommunication, non-destructive inspection and quality control, a large variety of terahertz emitters and detectors are proposed and demonstrated.

Meanwhile, thanks to energy level engineering in intersubband transition, novel optoelectronic devices have been developed and investigated. Quantum Well Infrared Photodetector (QWIP) and Quantum Cascade Laser (QCL) are two typical examples based on intersubband transition.

In quantum well structure, energy level engineering enable tuning the operating wavelength of devices, either for absorption or emission, over a large range especially in infrared (IR).

In the past decades, tremendous research on QWIP based on III-V material proved it to be a flexible and high-speed photodetector, with advantages of easy integration and multicolor application, in the mid-wavelength infrared (MWIR, 3-5 μm) and long-wavelength infrared (LWIR, 8-12 μm) atmospheric spectral windows [1]–[3].

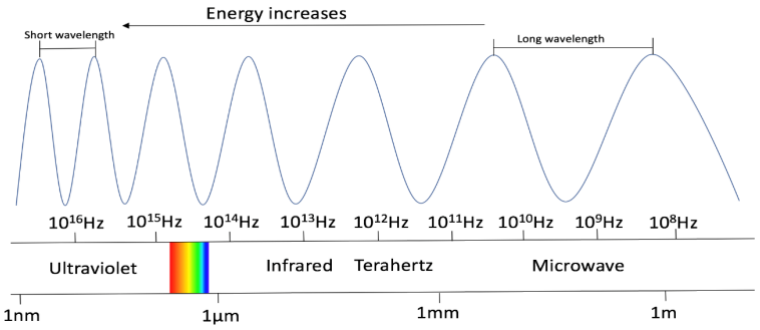

Figure 1.1 Electromagnetic spectrum

According to the electromagnetic spectrum shown in Figure 1.1, terahertz range falls in between infrared and microwave regions. People had not realized the presence of terahertz radiation in everyday life for a long time, not only because of its high frequency which cannot be detected by electronic counter, but also due to strong absorption by water in the air. Technology that utilizes terahertz radiation, especially those involve its generation and manipulation, is still in its infancy.

Electromagnetic waves at terahertz frequencies, alike those at infrared and visible light wavelengths, propagates mainly along a line-of-sight. In addition, terahertz radiation is non-ionizing (thus environmentally-friendly and safe to human body) due to their relative low photon energy. On the other hand, terahertz waves, similar to microwaves and radio frequency waves,

can penetrate non-metallic materials which are typically opaque in infrared region. More terahertz technologies are finding their ways in practical applications.

Terahertz technology has long been investigated but detecting terahertz wave is still quite challenging. There is a large variety of potential application fields for terahertz detectors, such as security, spectroscopy, imaging and wireless communications. Terahertz quantum well photodetector (THz QWP), first proposed by H.C.Liu in 2004 [4], is one of the detectors that have been demonstrated working in the terahertz region. Based on the III-V semiconductor material systems, it benefits from mature growth techniques by using MBE. As a photonic detector, it has proved its fast optical response speed in GHz [5] and can be applied in ultrafast spectroscopy and beatnote detection. Nevertheless, THz QWPs at low frequency range around 3 THz are rarely reported due to high requirement of MBE growth quality which comes from ultralow aluminum fraction in quantum barrier regions, and poor temperature performance. This thesis aims for developing a THz QWP targeting at 3 THz as well as a comprehensive simulation and characterization system. Moreover, simulation models of different light couplers are also to be investigated so, in the future, they can be integrated with THz QWPs and improve the detector performance.

1.2 Literature Review

1.2.1 Terahertz Radiation Applications

Terahertz radiation has been acknowledged to be a good candidate in many applications because of its attractive and unique properties. One of the primary applications with terahertz radiation is spectroscopy [6] in material research. It was realized in early days of far-infrared spectroscopy that terahertz wave yields strong optical resonance in molecular crystals [7]. Terahertz wave can interact strongly with materials or systems that have energetic transition in meV range and characteristic lifetime in picosecond range. Furthermore, in terahertz time-domain spectroscopy, electric field rather than just power of the pulse is measured, thus the uncertainty of Kramer-Kronig analysis is eliminated compared with other spectroscopy techniques [8].

In addition to spectroscopy, terahertz imaging is also one of the most important applications of terahertz wave. Terahertz radiation, compared with many other wavelengths of light, has several advantages when used in imaging. Many materials are transparent to terahertz waves, including plastics, paper, wood and fabrics. Therefore, items of interest, such as chemical spices, can be detected through layers that are visually opaque. Foremost, terahertz can excite vibrational modes inside both inorganic and organic materials, which motivates the application of terahertz imaging in distinguish chemicals based on their composition and crystalline structure. Due to its shorter wavelength, terahertz imaging benefits from better spatial resolution comparing to microwave frequencies. However, it is still not sufficient for application in nanoscale. To overcome this limitation, a large variety of methods has been applied, including scanning near-field microscopy, one of the potential nanoscale imaging system based on terahertz wave modulation [9].

When comparing to high energy X-ray imaging (energy in the range of 100 eV to 100 keV), terahertz imaging (in meV) is environment-friendly to human being and nature due to its non-ionizing property. Monitoring water level in plants, defects in products such as building blocks and film-coated tablets have been already performed using terahertz imaging [10], [11]. However, atmospheric water absorption in terahertz range is one limiting factor for application in long-distance imaging or detection. To realize all the applications mentioned above, it is important to develop high-performance THz detectors.

1.2.2 Terahertz Detectors

Since terahertz radiation has been one of the most attractive research these days, there are a large variety of terahertz detectors that has been demonstrated, including optoelectronic quantum devices, carbon nanotube and nanowire, field effect transistors as well as room temperature bipolar semiconductor bolometers which based on hot electron [12], [13].

Most of the terahertz detectors can be classified in subcategories based on their principle: direct detection, including thermal and photonic detectors, and heterodyne detection.

Thermal detectors: Golay cells [14], [15], pyroelectric detectors [16], different kind of thermal direct detection detectors (bolometers and microbolometers, illustrated in Figure 1.2) [17], [18], are typical thermal detectors in terahertz range. Measurable temperature change is produced by

incoming photons in thermal detectors, by which light is detected quantitatively. Thermal detectors can achieve room temperature operation, but they usually suffer from long response time and poor sensitivity.

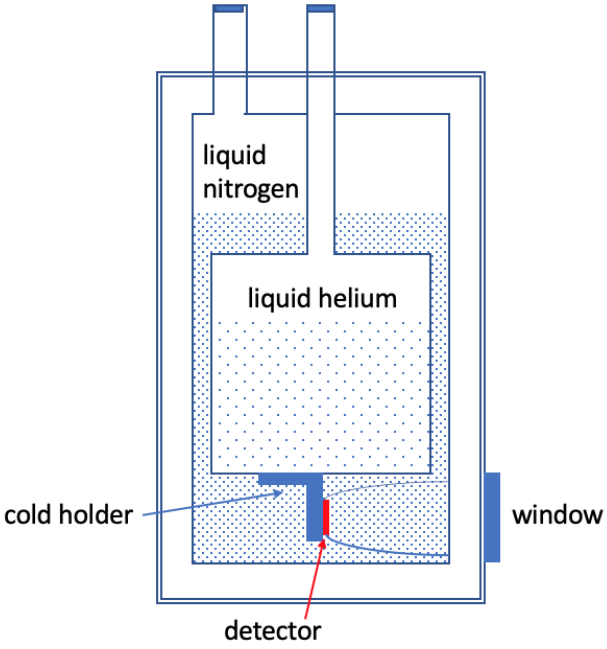

Figure 1.2 Schematic of bolometer

Photonic detectors: Photonic detectors includes Silicon(Si), Germanium (Ge), Indium Antimonide (InSb) and Gallium Arsenide (GaAs) devices. For those devices, incoming photons interact with carriers in material, which produce measurable photocurrent or photovoltage. Compared with thermal detectors, photonic detectors yield fast response ($\tau \approx 10^{-6}$~10^{-8} s) and better Noise Equivalent Power ($NEP \approx 10^{-13}$~5×10^{-17} W/Hz$^{1/2}$). However, they usually operate at low temperature ($T \leq 4$ K).

Heterodyne Detectors: Heterodyne detection in terahertz region converts terahertz frequencies down to intermediate frequencies by different photomixing (illustrated in Figure 1.3).

Heterodyne detectors include devices such as Schottky diode Mixer (SDM), Superconductor-Insulator-Superconductor Mixer (SISM) and Hot Electron Mixer (HEM). By interacting two base signals together, whose frequencies f_1 and f_2 are different but close, they can produce two other signals of frequencies $f_- = |f_1 - f_2|$ and $f_+ = |f_1 + f_2|$. Signal f_- can fall in the THz domain for THz applications if two base signals are in gigahertz region. One of the primary advantages is that measuring through lower frequency can be more suitable for electronics time response.

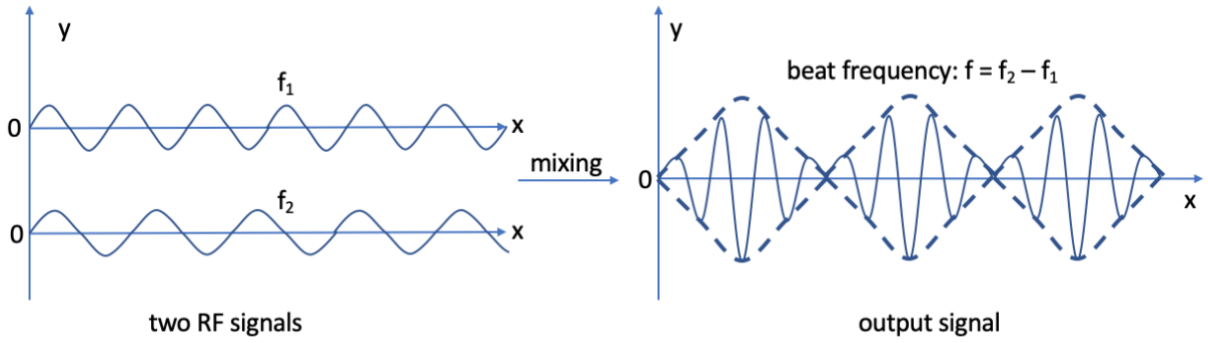

Figure 1.3 Schematic of photomixing

1.2.3 Quantum Well Infrared Photodetectors

Boosted by the development of intersubband transitions, a large variety of novel optoelectronic devices with quantum well structure have been invented, such as QCL and QWIP. QWIP devices are usually based on GaAs/$Al_xGa_{1-x}As$ material system and designed for and absorption range of 3-14 μm by energy level engineering. Compared with HgCdTe and InSb, two of other typical photodetectors working in the same spectrum region, QWIP benefits from the maturity of the

growth and fabrication process using GaAs/$Al_xGa_{1-x}As$ material system. In addition, its fast response, potential in system integration and multicolor application make QWIP a perfect candidate in imaging and high-speed telecommunication.

Different active region designs can achieve not only tunable absorption wavelength, but also multiple transition mechanisms. There are two types of QWIP devices with different mechanism: photoconductive QWIP and photovoltaic QWIP. The primary difference is that photoconductive device need bias for light absorption whereas photovoltaic device can operate under zero bias.

In traditional photoconductive QWIP devices, one module only contains a single quantum well, separated by thick quantum barriers. Photocurrents are generated by incoming photons interacting with electrons in the ground state, further exciting them into a state of higher energy. Figure 1.4 shows a schematic of one quantum well in QWIP. Impinging photons are absorbed by the quantum well, thus electrons in the ground state are excited into the upper energy level or the continuum, which contributes to a photocurrent. In addition to the photocurrent, there is also a dark current flowing through the continuum, which is the current in absence of any incoming light. Asymmetric quantum structure which can tune the spectrum linewidth has also been reported [19].

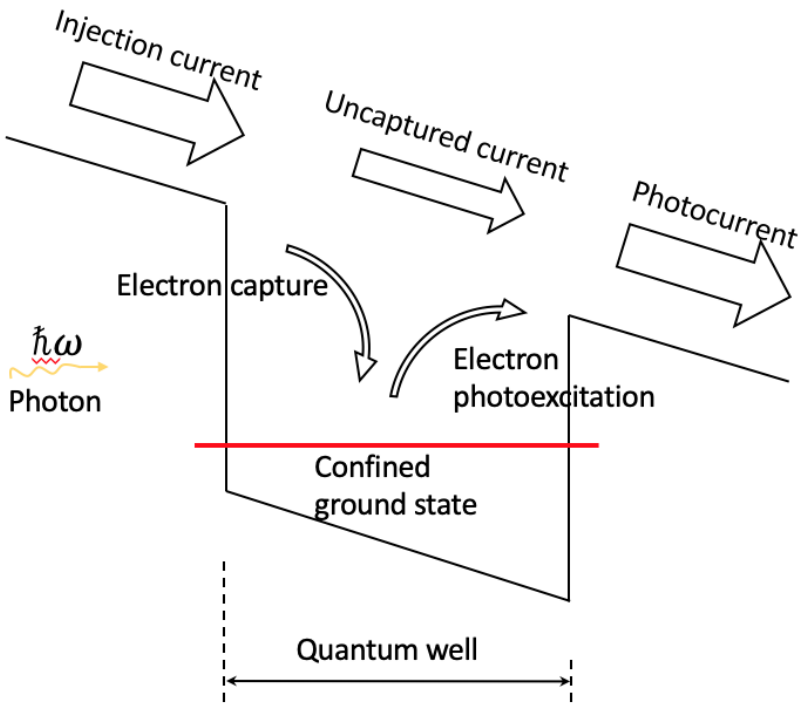

Figure 1.4 Schematic of single module in QWIP, showing the electron capture and excitation processes

Photoconductive QWIP is implemented to achieve good detector responsivity, but on the other hand, it will cause high dark current induced by external electric field. To tackle this issue, photovoltaic devices are designed with zero operating bias. In photovoltaic QWIP, thickness of the quantum barrier is reduced to couple energy states in different module together, extending into the entire active region. Both ground and excited localized states form minibands, in which electrons will flow. To collect the electrons in upper miniband, different strategies have been applied. Graded collectors (Figure 1.5(a)) were first applied, but replaced by square collectors (Figure 1.5(b)) afterwards due to the leakage current from lower miniband to the collector.

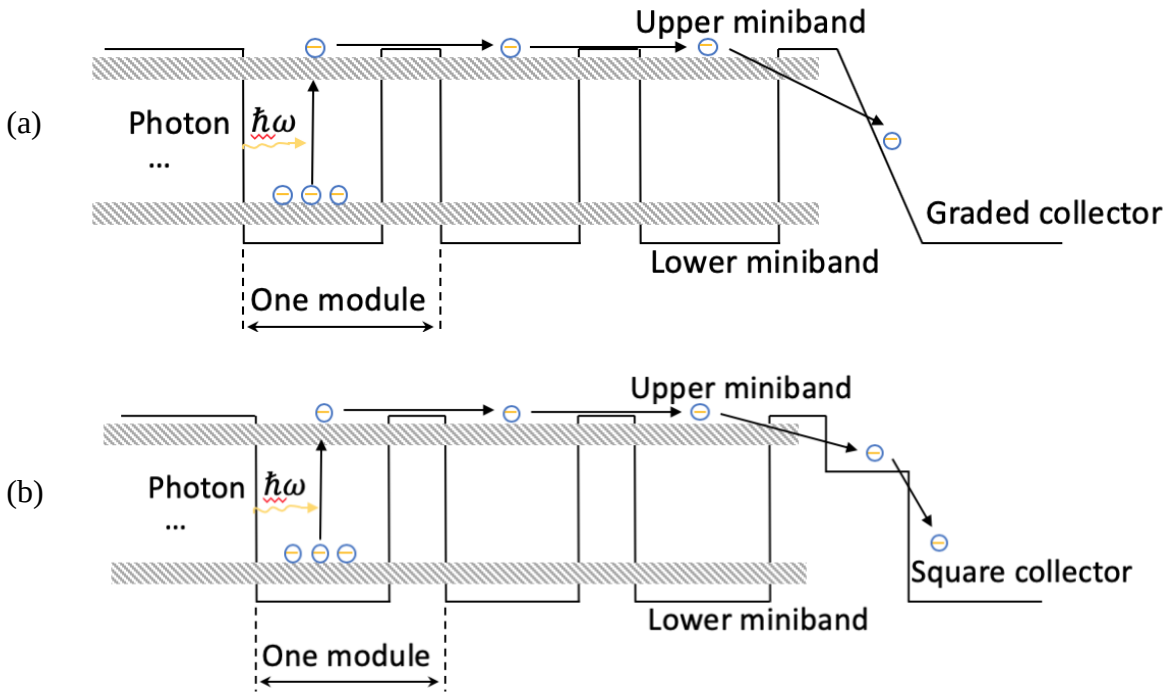

Figure 1.5 Energy band diagram of photovoltaic QWIP with (a) graded collector; (b) square collector

To reach high detectivity as well as responsivity, Schneider [20] proposed a photovoltaic QWIP based on four-zone scheme. In their design (Figure 1.6(a)), each module consists of four zones, namely an emission zone, drift zone, capture zone and tunneling zone. Each zone can be designed independently. This design achieved similar detectivity compared with photoconductive device, and was later applied in dual-color application in Long-Wavelength Infrared (LWIR) and Mid-Wavelength Infrared (MWIR) region [21].

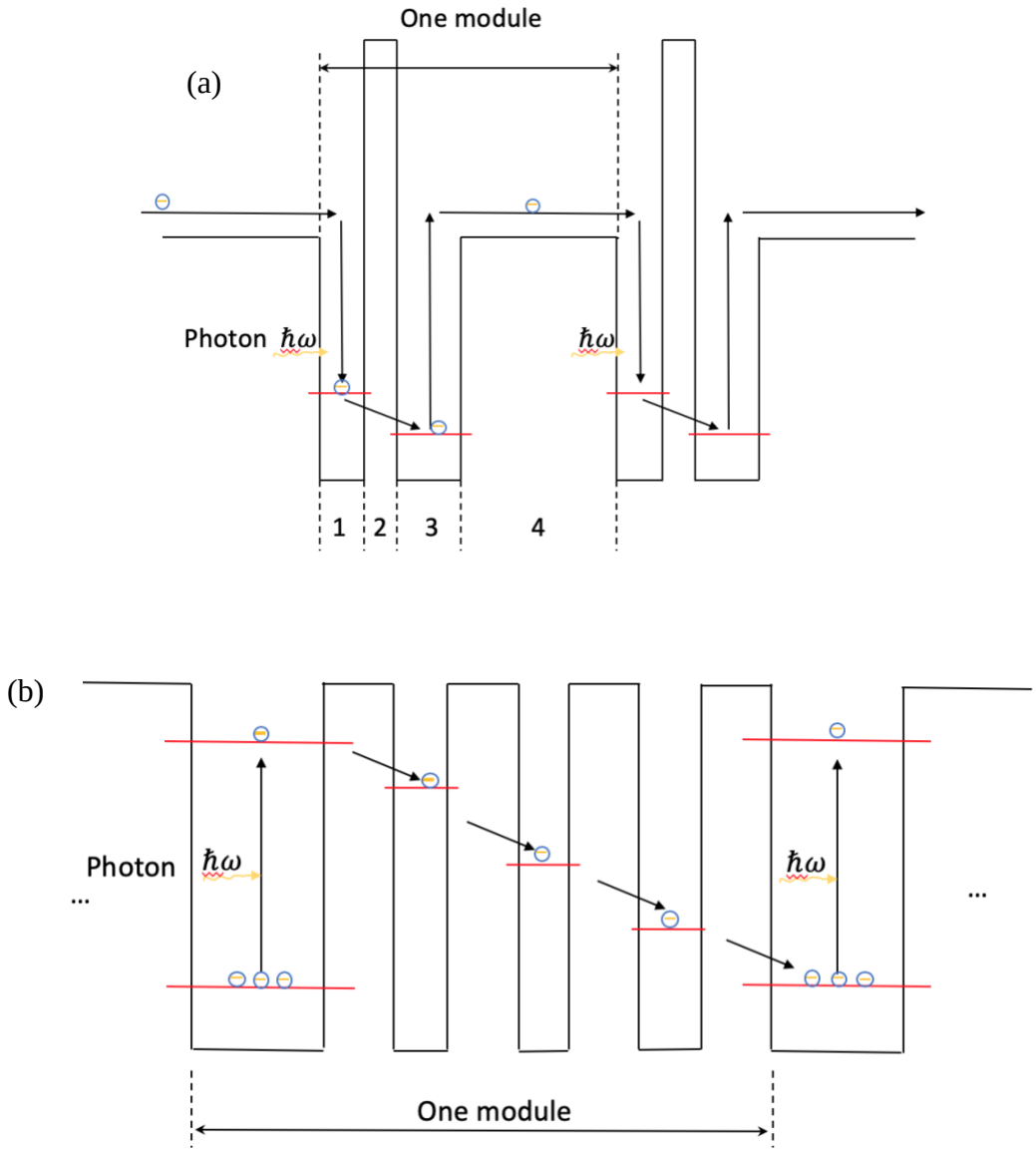

Figure 1.6 Energy band diagram of (a) photovoltaic QWIP with four-zone scheme, 1: capture zone, 2: tunneling zone, 3: emission zone, 4, drift zone; (b) QCD

There are many other designs of QWIPs as well. Proposed by Gendron [22], Quantum Cascade Detector (QCD) has become one of the promising design recently. As pointed out in an review paper [23], the QCD has shown to be a robust design from near-infrared to terahertz region. In a QCD, rather than extracted to the next module via the continuum, electrons tunnel through a series cascade quantum wells until it reaches next module (Figure 1.6(b)). In addition, QWIP

integrated with digital graded superlattice barrier [24] or dot-in-a-well (DWELL) infrared photodetectors [25] have also gained lots of interest in the past decades.

1.2.4 Terahertz Quantum Well Photodetectors

In 2004, Liu [4] and Graf [26] respectively realized THz wave detection using a QWP structure based on GaAs/$Al_xGa_{1-x}As$ material system. Liu [4] proposed a THz QWP based on single well structure, managed to reach 0.6 A/W at peak response wavelength of 42 μm (7.1 THz) for temperature lower than 20 K, while Graf [26] chose QCD structure, achieving responsivity of 8.6 mA/W at peak response wavelength of 84 μm (3.57 THz). However, studies in THz QWP based on QCD has not been much pushed further since then, despite of its relatively low dark current. Compared with the other, single well structure THz QWP is continuously attracting research interests, benefiting from its higher responsivity and intuitive design process. Many bound-to-quasibound THz QWP devices using single well structure have been studied. New designs of active region and light coupler were proposed by Cao [27] in 2011 and Guo [28] in 2013, respectively.

Applications based on THz QWP are still in their preliminary stages. One of the performance-limiting factors of THz QWPs is that its operating temperature is very low – down to 10 K in most cases. Many researches have been done aiming at realistic applications. THz free-space communication, operating at 3.8 THz, using THz QCL as emitter and THz QWP as receiver has

been demonstrated [29], [30]. Besides, THz imaging experiments have proved that THz QWP can be a good candidate detecting concealed metal objects [31], [32].

There are also other material systems investigated to be applied in THz QWP. For instance, GaN/$Al_xGa_{1-x}N$ has been studied from 2013 as an alternative material system [33], [34], which is expected to absorb the wavelength in the GaAs/$Al_xGa_{1-x}As$ Reststrahlen forbidden band (5-12 THz). THz QWP based on GaN material system can work with an even higher response speed and potentially in room temperature region according to theoretical anticipation. However, GaN/$Al_xGa_{1-x}N$ device is suffered from poor growth quality, which is yet to be improved in the future.

Recently, different light-coupling structures has been studied to boost device performance of THz QWPs [35]. Due to the polarization rule, only the light with an electric field along the growth direction can be absorbed by intersubband transition. Traditionally, QWIP devices as well as THz QWPs use 45° facet for light coupling (Figure 1.7), which is not applicable for imagers such as focal plane arrays (FPAs) or large-scale integration on Silicon chips.

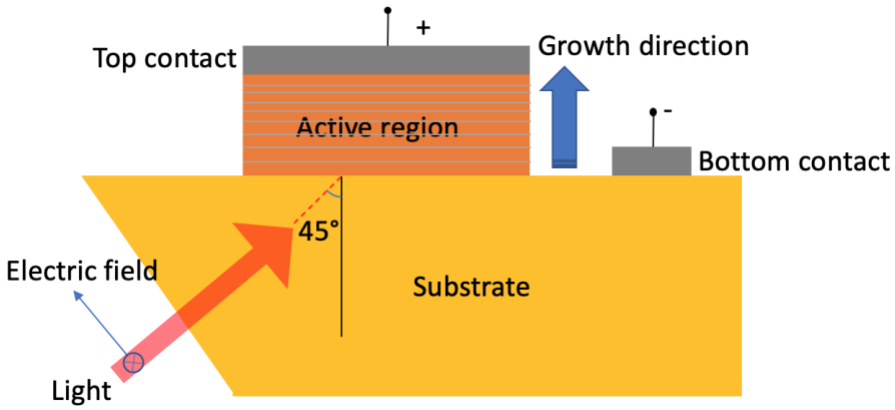

Figure 1.7 Schematic of THz QWP with 45° facet

To realize normal incidence operation, several studies that implements different light-coupling schemes have been conducted and significantly improve device performance. Zhang reported a THz QWP implemented with metal grating couplers and improved device responsivity by up to 150% [36]. THz QWPs integrated with a patch antenna has been demonstrated an impressive six-fold improvement compared their counterparts with traditional 45° facet coupling [37]. In addition, many other light-coupling structures have been proposed to be applied as well, including meta-atoms [38] and LC circuits [39]. Recently, impressive results have been demonstrated by Palaferri [40], showing that double metal patch antenna enables room temperature operation of QWIP devices in mid-infrared region, setting a good example for potential implementations in THz QWP devices to increase their operating temperature.

1.3 Research Objectives

THz QWPs, especially at low frequency around 3 THz, have many potential applications, such as imaging, spectroscopy and communication. Nevertheless, they cannot be widely used due to their limited performance, particularly low operating temperature and poor signal-to-noise ratio at higher temperature. Moreover, THz QWPs absorbing at 3 THz are still undeveloped and the lowest response demonstrated so far is 3.24 THz by H.C.Liu [41]. As such, a new THz QWP targeting at 3 THz is to be fabricated and tested. A double patch antenna structure, which shows very promising potential in enhancing THz QWP temperature performance, is discussed and simulated in preparation for being implemented with THz QWP devices.

1.4 Thesis Overview

This thesis focuses on simulation and characterization of traditional photoconductive THz QWP at THz frequencies lower than the Reststrahlen band. Furthermore, different light coupling structures will be introduced and numerical modeling results will be presented.

Chapter 2 explains the physics and theory of traditional THz QWP, highlighting all the figures of merit that dictate device performance: absorption intensity and spectrum, photocurrent and responsivity, detectivity, dark current and operating temperature. Many-body effect, which plays a crucial role in THz QWP, will be discussed as well. Moreover, a simulation model is proposed and compared with published data from different literatures for validation. Characterization setup and results are also included in this chapter. Working device has been demonstrated with BLIP temperature of 10 K, detectivity up to 4.63×10^{10} $cmHz^{1/2}/W$ and absorption range from 94.5 cm^{-1} (2.83 THz) to 142.7cm^{-1} (4.25 THz) and peak at 107.32 cm^{-1} (3.22 THz).

Chapter 3 theoretically describes the mechanism of a 1D metal grating coupler and patch antenna structure in THz QWPs. Numerical solutions are presented with simulated electric field patterns, coupling efficiency and reflection, which agree with rules of thumb.

Important information about device growth, fabrication and packaging process traditional 3THz photoconductive QWP is included in appendices.

Overall, a comprehensive study of THz QWP, including theoretical principles, simulation models, characterization setup and analysis on testing results, is reported in this thesis. Numerical solutions on light coupling structures are presented as well and can be further implemented in THz QWPs in future research. THz QWP working at 3 THz is challenging to achieve because of high requirements in the MBE growth and characterization systems. Tested THz QWP manages to realize low frequency absorption near 3 THz, and will have strong potentials in either further improving its performance by implementing light coupling structures or combining with THz QCLs at similar emission wavelength for applications in spectroscopy or wireless communications.

Chapter 2 Terahertz Quantum Well Photodetector

Terahertz QWPs are photodetectors that are based on intersubband transition between two discrete energy levels which locate in conduction band of quantum well heterostructures. The heterostructure is designed so that the excited electrons can escape and generate photocurrent flow. This chapter describes the development of physical model and characterization of THz QWP and covers the analysis on simulation results and important figures of merit of fabricated THz QWP device.

2.1 Active Region Model

Active region consists of quantum well heterostructures where intersubband transition happens. It determines the absorption energy as well as flowing dark current at given bias voltage; and it is the fundamental theory on how QWIP and THz QWP work. In typical QWIP devices, active region is made of consecutive III-V layers grown by molecular-beam epitaxy (MBE). The band gap difference in heterostructures can form quantum wells in conduction or valence band, which leads to confinement of carriers and discrete energy bands. THz QWP utilizes the energy transition between two subbands inside quantum wells, which is called intersubband transition. Unlike QWIPs, which target at mid-infrared absorption with energy of hundreds of meV, THz QWPs are designed to have their energy bands separation around tens of meV in order to absorb terahertz wave. Therefore, quantum wells in THz QWP are designed to be shallower by reducing the dopant proportion in the quantum barrier region (aluminum fraction in typical $GaAs/Al_xGa_{1-x}As$ material system, usually from 1.5% to 5%) compared with QWIP devices (aluminum fraction higher than 10%). Moreover, there are multiple many body effects (to be discussed in section 2.1.3) which tilt conduction band by a few meV can significantly change the intersubband transition energy and need to be considered in simulation of active region in THz QWPs.

2.1.1 Quantum Well Heterostructures

The quantum well heterostructure (shown in Figure 2.1) is the core in designing the active region model of THz QWP. It determines the absorption wavelength range as well as absorption coefficient. The distribution of carriers in the heterostructures can be engineered by tuning the

potential profile, which forms multiple discrete energy states. As a result, carriers can be confined at certain energy levels between which optical absorption is observed.

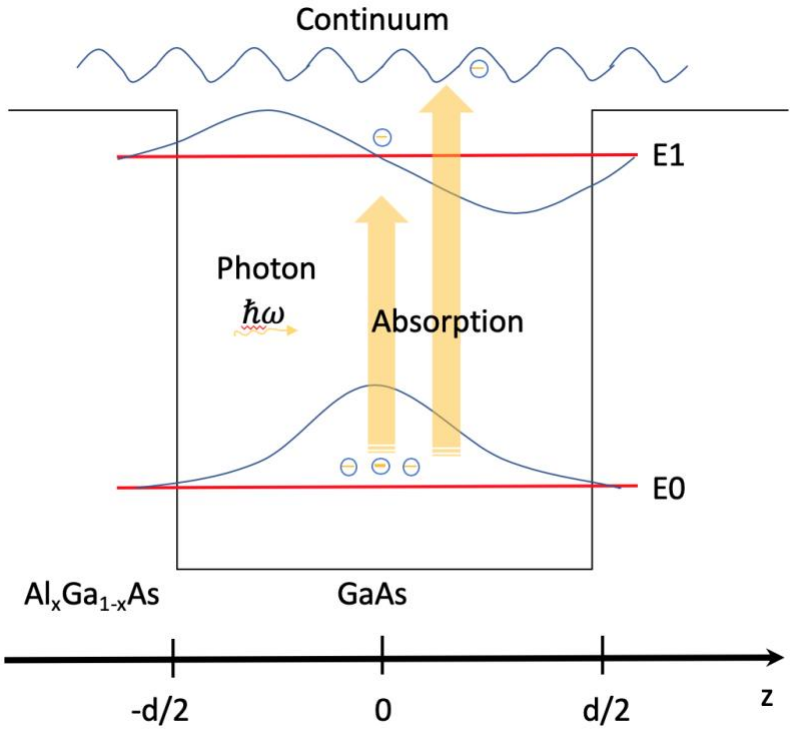

Figure 2.1 Schematic of quantum well heterostructure, E_0: ground energy state, E_1: first excited energy state

The energy states and wavefunctions of the active region are calculated from the Schrödinger equation:

$$-\frac{\hbar^2}{2m_e}\nabla^2\Psi(r) + V(r)\Psi(r) = E\Psi(r) \qquad (2.1)$$

where E and $\Psi(r)$ are the energy states and corresponding wavefunctions, respectively. m_e is the effective mass of the electron, $\hbar$ is the reduced Planck constant, $V(r)$ is the potential profile, which takes account of band offset, external electric field and many-body effect (section 2.1.3).

To construct the active region model, an approximation on the potential profile is fundamental for calculating the energy states and wavefunctions. The material system we choose is n-type

GaAs/$Al_xGa_{1-x}As$, with GaAs as the quantum well layer and $Al_xGa_{1-x}As$ as the barrier layer. Since the intersubband transitions solely happen in the conduction band, we need to first determine the height of the barrier, which is the conduction band offset between two different layer. This offset is approximated by [42]:

$$\Delta E_c = 0.904x(eV) \tag{2.2}$$

where x is the fraction of aluminum in $Al_xGa_{1-x}As$.

Besides, the effective mass in each layer is also determined by the fraction of aluminum, as $m_w = 0.067m_0$ in GaAs and $m_b(x) = (0.067 + 0.083x)m_0$ in $Al_xGa_{1-x}As$.

The number of module in THz QWP is mainly constrained by growth quality. Too much thickness will cause growth strain and defects which damage device performance. Thus, target device total thickness is chosen to be around 3.5 μm in order to maximize the absorption strength. Then the number of module can be calculated accordingly.

Doping profile for simulating the energy state and wavefunction is set to be the traditional uniform central doping in well region. The doping concentration is given by [42]:

$$E_f = C_f k_B T \tag{2.3}$$

$$N_{2D} = \frac{m_e E_f}{\pi \hbar^2} = \frac{C_f m_e k_B T}{\pi \hbar^2} \tag{2.4}$$

where E_f is the Fermi level of the device, T is the temperature, k_B is the Boltzmann constant, and C_f is a constant in the equations. N_{2D} is the two-dimensional doping density that determines the Fermi level. N_{2D} can be chosen as different values to set the C_f, which is 1 for maximizing

background-limited operating temperature (BLIP temperature) or 2 for optimizing dark current limited detectivity [42].

2.1.2 Intersubband Transition

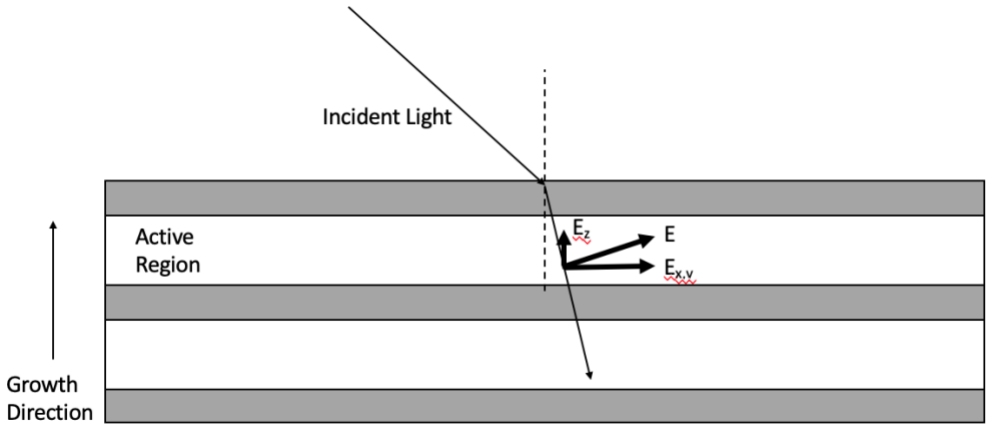

Figure 2.2 Schematic of Intersubband transition selection rule, only the component of the electric field of incident light that is parallel to growth direction can be absorbed by active region [43]

Intersubband transition happens between two discrete energy states, which is called subbands, within the conduction band of semiconductor heterostructures. To quantify intersubband transition in active region model, Fermi's golden rule is applied:

$$W_{i\to f} = \frac{2\pi}{\hbar}|\langle f|H'|i\rangle|^2\delta\left(E_f - E_i - \hbar\omega\right) \tag{2.5}$$

where $W_{i\to f}$ is the transition rate from initial state $|i\rangle$ to the final state $|f\rangle$, with energy E_i and E_f respectively. $\langle f|H'|i\rangle$ is the matrix element of the interaction Hamiltonian between final and initial states.

The interaction Hamiltonian is given by:

$$H'(r) = -\frac{eA_0 e^{ik_{op}r}}{2m_0}\hat{e}\cdot pe^{-i\omega t} - \frac{eA_0 e^{-ik_{op}r}}{2m_0}\hat{e}\cdot pe^{i\omega t} \quad (2.6)$$

where A_0 is the amplitude of the potential vector, k_{op} is the wavevector of the radiation, $\hat{e}$ is represents the unit vector along the direction of electric field and p is the momentum vector. Therefore, the absorption transition rate can be written as:

$$W_{i\to f}^{abs} = \frac{2\pi}{\hbar}\left|H'_{fi}\right|^2 \delta\left(E_f - E_i - \hbar\omega\right) \quad (2.7)$$

where $H'_{fi} = -e\langle f|e\boldsymbol{r}\cdot\boldsymbol{E}|i\rangle$.

According to the equations above, $W_{i\to f}^{abs} = 0$ if $H'_{fi} = 0$, which stands for the situation where incoming light is parallel to the growth direction of THz QWP. This absorption selection rule indicates that the incoming light can be absorbed only if its electric field has the component along the quantum well direction, as shown in Figure 2.2, which has practical implication on the geometry of how IR detector based in intersubband transition is built.

Oscillator strength is one relevant quantity in intersubband transition. In the active region model of THz QWP, all the carriers are located in ground energy state initially. Therefore, only oscillator strength between certain excited state and ground state is calculated [42]:

$$f_{1,n} = \frac{2m_e E_{1,n}}{\hbar^2}\left|\langle\Psi_n|\hat{z}|\Psi_1\rangle\right|^2 \quad (2.8)$$

where Ψ_n is the wavefunction of the nth energy state and $\hat{z}$ is the operator. This equation is valid given uniform effective mass across barrier layers.

In active region model, the absorption coefficient of intersubband transition is derived from Fermi's golden rule. It is defined as the ratio of the absorbed energy per unit time, area and the radiation intensity of incident light, between the ground state and all excited states [42]:

$$\eta(\omega) = \frac{e^2 h N_{2D}}{4\pi\varepsilon_0 n_r m_e c} \frac{sin^2\theta}{cos\theta} \sum f_{1,n} \frac{\Delta E}{\left(E_{1,n} - \frac{h\omega}{2\pi}\right)^2 + (\Delta E)^2} \tag{2.9}$$

where n_r is the refractive index of GaAs and N_{2D} is the sheet doping density. ΔE represents the broadening of the absorption of spectrum and θ is the incident angle of impinging light. $E_{1,n}$ and $f_{1,n}$ represent the energy difference and oscillator strength between the ground state and the nth energy state respectively. The absorption spectrum given by (2.9) is treated as a Lorentzian line shape with broadening of ΔE, which is usually a few meV in THz QWP.

2.1.3 Many-body Effect

Many-body effect, first reported by Graf [44], tends to play a more important role in a THz QWP than a QWIP in mid-infrared region. Because of the relatively small barrier height that comes from low aluminum fraction, the energy states and peak absorption wavelength become more sensitive to the variation in potential profile. Therefore, many-body effect needs to be taken into account in the active region model of THz QWP [45].

With many-body effect included, the potential profile in (2.1) can be expanded as [42]:

$$V(r) = V_{cr}(r) + V_H(r) + V_{xc}(r) + eFz \tag{2.10}$$

V_{cr} represents the ideal potential profile determined by quantum well structure, V_H is the Hartree potential, V_{xc} is the exchange-correlation potential and the term eFz stands for the voltage drop

resulting from external bias. V_H and V_{xc}, caused by electron gas and ionized donors, are the two main components that need to be considered in many-body effect.

Given $n(z)$, the electron distribution can be expressed as [42]:

$$n(z) = \frac{m_e k_B T}{\pi \hbar^2} \sum_i \ln\left(1 + e^{\frac{E_f - E_i}{k_B T}}\right) |\Psi_i(z)|^2 \tag{2.11}$$

Hartree potential can be approximated using local carrier density, which is related to the doping profile and electron distribution [44], [46]:

$$V_H(z) = \frac{e^2}{\varepsilon_s \varepsilon_0} \int_{-\infty}^{z} (z - z')\big(N_D(z') - n(z')\big) dz' \tag{2.12}$$

where ε_s and ε_0 are the static and vacuum permittivity respectively, $N_D(z)$ represents the doping profile and $n(z)$ is the electron distribution. E_i the i[th] bound state, $\Psi_i(z)$ is the i[th] wavefunction.

Exchange-correlation potential is solely dependent on electron distribution which cannot be controlled by designing [47]:

$$V_{xc} = -\frac{2}{\pi \gamma r_s}\left(1 + \frac{B r_s}{A} \ln\left(1 + \frac{A}{r_s}\right)\right)(Ry) \tag{2.13}$$

where $\gamma = (9\pi/4)^{-1/3}$, $r_s = \frac{m_e}{m_0 \varepsilon_s}(4\pi n(z)/3)^{-1/3}$, $A = 11.4, B = 0.6213$.

In addition to these two static effects that comes from local carrier density, there are also other dynamic factors that contribute to many-body effect. The approximated transition energy is then given by [42]:

$$E'_{21} = E_{21}\sqrt{1 + \alpha - \beta} \tag{2.14}$$

$$\alpha = \frac{2e^2 N_{2D}}{\varepsilon_s \varepsilon_0 E_{12}} \int_{-\infty}^{+\infty} \left(\int_{-\infty}^{z} \Psi_2(z') \Psi_1(z') dz' \right)^2 dz \tag{2.15}$$

$$\beta = -\frac{2N_{2D}}{E_{12}} \int_{-\infty}^{+\infty} dz \, \Psi_2(z)^2 \Psi_1(z)^2 \frac{\delta V_{xc}(n(z))}{\delta(n(z))} \tag{2.16}$$

where E_{21} and E'_{21} are transition energy with or without correction by dynamic effects. Coefficients α and β represents depolarization and excitation shift and N_{2D} is the two-dimensional sheet carrier density.

2.2 Photoconductive THz QWP

Typical photoconductive THz QWP contains multiple periods with only one quantum well in each period. Therefore, it is a symmetric material in terms of its electrical characteristics. There are multiple aspects need to be considered when designing a THz QWP. Carrier transport mechanism plays a crucial role in determining detector's dark current, which then affects the macroscopic figures of merit of the detector, including responsivity and detectivity. Furthermore, light coupling strategy is also necessary in photoconductive THz QWP due to the selection rule of intersubband transition.

2.2.1 Optimum Electronic Confinement

The first QWIP device was proposed by Levine [1] in which both ground state and excited state are confined in the quantum well. QWIPs with this bound-to-bound transition suffer from

complex tunneling process and show a nonlinear behavior of dark current and responsivity (Figure 2.3(a)). By reducing the quantum well width, excited states can be pushed into continuum band, which makes bound-to-continuum transition happen. In this case, excited carriers can flow through the active region without tunneling through quantum barriers, which generates more photocurrent (Figure 2.3(b)). On one hand, the design with bound-to-bound transition can strengthen the absorption but suffers from a low escape efficiency as well as a narrow absorption peak . On the other hand, the bound-to-continuum design makes the escape efficiency higher and the absorption spectrum broader; nonetheless, the absorption becomes weaker.

Firstly demonstrated by Gunapala and Bandara [48], bound-to-quasibound transition (Figure 2.4) significantly improve device performance by aligning the first excited state with the top edge of quantum well. As a result, the working bias is reduced so that the dark current is minimized. This design shows a high absorption and a high escape efficiency at the same time and it is implemented to realize optimum electron confinement in QWIP, as well as THz QWP.

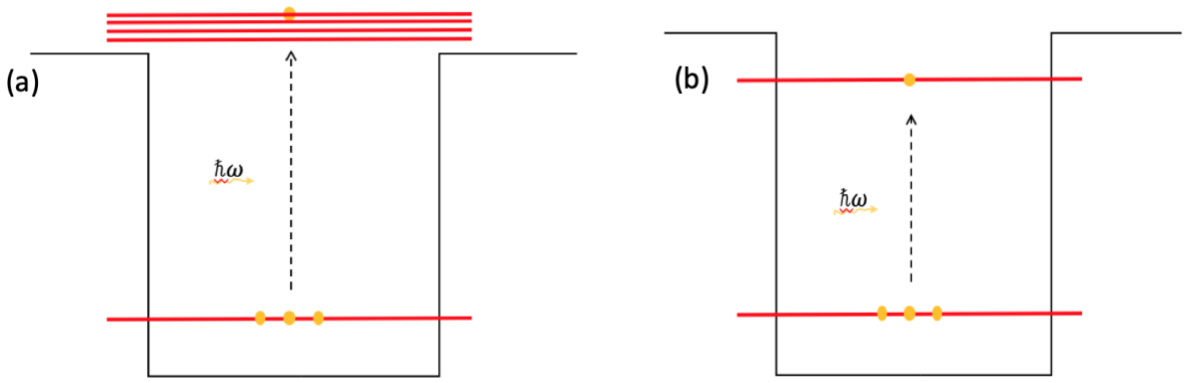

Figure 2.3 (a) bound-to-continuum (b) bound-to-bound intersubband transition

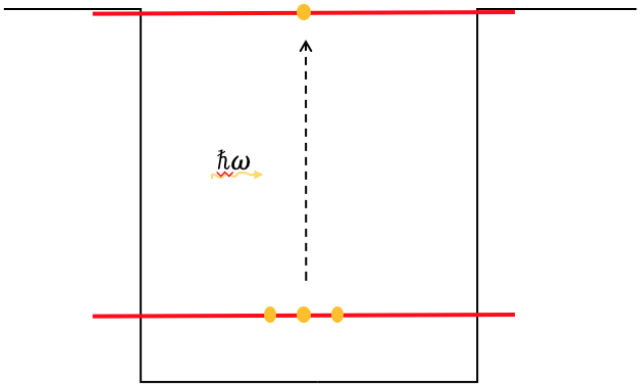

Figure 2.4 bound-to-quasibound intersubband transition

2.2.2 Photocurrent Transport

There are several models that have been applied in photoconductive THz QWPs. In this thesis, we are referring the emission-capture model [49] in simulating photocurrent transport. By introducing the capture and emission probabilities of electrons, this model can explain how the current flows through each quantum well. Considering the conservation law of flowing current under steady state, we have [42]:

$$J = j_e + (1 - p_c)J \tag{2.17}$$

where J is the current flowing through the active region, j_e is the current emitted from the well and p_c is the capture probability. Visualization of this model is shown as Figure 2.5

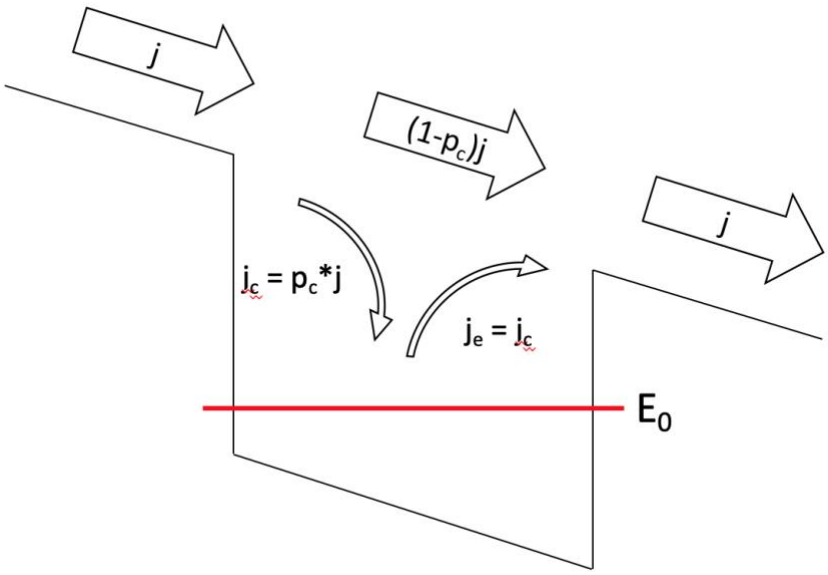

Figure 2.5 Schematic diagram of carrier transportation in THz QWP, j: total current; j_c: captured current; j_e: emission current; p_c: capture probability

When the incoming photon is absorbed, it contributes to direct photoexcitation of the electrons from quantum well and leads to extra injections from contact to balance the loss the emitted electrons.

The gain of single quantum well can be expressed by the ratio between the probability of emission from the well and capture probability [42]:

$$g = \frac{p_e}{p_c} \tag{2.18}$$

where g is gain and p_e is emission probability. Two scenarios will be considered in photocurrent transport model for THz QWP: under dark condition and IR illumination.

Under dark condition, thermionic emission, direct tunneling and thermo-assisted tunneling are three main mechanisms in typical QWIP devices (shown in Figure 2.6). In a bound-to-

quasibound THz QWP, direct tunneling is mostly smaller due to thick barriers. To calculate the dark current density J_{dark}, capture probability p_c needs to be considered [42]:

$$p_c = \frac{\tau_{trans}}{\tau_{trans} + \tau_c} \tag{2.19}$$

where τ_{trans} represents the transit time for electrons travel through one quantum well region, and τ_c is the capture time for excited electrons being captured back into the well. For actual device under operating electric fields, we usually have $\tau_c \gg \tau_{trans}$, which means $p_c \ll 1$. Therefore, the dark current density J_{dark} in THz QWP becomes [42]:

$$J_{dark} = e\frac{N_{2D}}{L_p}\frac{\tau_c}{\tau_{scatt}}v(F) \tag{2.20}$$

where L_p is the period length per module and equals the sum of well width and barrier width ($L_p = L_w + L_b$). $v(F)$ is electron drift velocity, which is [42]:

$$v(F) = \frac{\mu F}{\left(1 + \left(\frac{\mu F}{v_{sat}}\right)^2\right)^{\frac{1}{2}}} \tag{2.21}$$

where F is the external electric field through active region, μ is the low field electron mobility and v_{sat} is the saturated drift velocity. The ratio τ_c/τ_{scatt} can be written as [50]:

$$\frac{\tau_c}{\tau_{scatt}} \approx \frac{m_b}{m_e} L_p \left(\frac{m_b k_B T}{2\pi\hbar^2}\right)^{\frac{1}{2}} \tag{2.22}$$

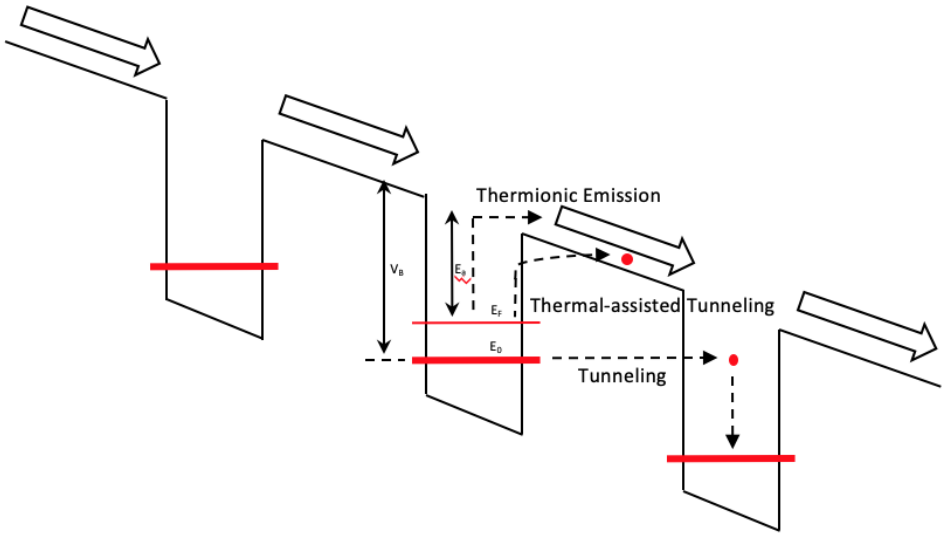

Figure 2.6 Schematic diagram of dark current components, there are three portions of dark current in THz QWP: 1 tunneling; 2 thermionic emission; 3, thermal-assisted tunneling

By taking transmission coefficient into consideration, we can put the estimated value of N_{2D} into (2.20) and J_{dark} becomes [50]:

$$J_{dark} = \frac{em_e}{\pi\hbar^2 L_p}\nu(F)\left(\frac{\tau_c}{\tau_{scatt}}\right)\int_{E_1}^{\infty} T(E,F)\left[1+\exp\left(\frac{E-E_f}{k_B T}\right)\right]^{-1} dE \qquad (2.23)$$

where $T(E,F)$ is the tunneling transmission probability and can be approximated by WKB approximation [50]:

for $E \geq E_b$,

$$T(E,F) = 1 \qquad (2.24)$$

for $E_b - eFL_b \leq E < E_b$,

$$T(E,F) = \exp\left[\left(-\frac{4}{3eF}\right)\left(\frac{2m_b}{\hbar^2}\right)^{\frac{1}{2}}(E_b - E)^{\frac{3}{2}}\right] \qquad (2.25)$$

for $E < E_b - eFL_b$,

$$T(E,F) = \exp\left\{\left(-\frac{4}{3eF}\right)\left(\frac{2m_b}{\hbar^2}\right)^{\frac{1}{2}}\left[(E_b - E)^{\frac{3}{2}} - (E_b - E - eFL_b)^{\frac{3}{2}}\right]\right\} \quad (2.26)$$

Total photocurrent can be calculated by [42]:

$$I_{photo} = e\eta\Phi g_{photo} = e\eta\Phi\frac{p_e}{Np_c} \quad (2.27)$$

where $g_{photo} = \frac{p_e}{Np_c}$ is the photoconductive gain of the active region and Φ is the incident photon flux, which is the number of photons per unit time. p_e and p_c are escape and capture probabilities respectively, given by (2.19) and [42]:

$$p_e = \frac{\tau_{relax}}{\tau_{relax} + \tau_{esc}} \quad (2.28)$$

One important conclusion drawn from the equations is that the photocurrent I_{photo} is independent of number of modules N and only determined by photoconductive gain of the active region and absorption. Since both factors play important roles, bound-to-quasibound is the best solution to maximize photocurrent. Either escape probability or absorption is low if it's bound-to-bound or bound-to-continuum design.

2.2.3 Responsivity

The Responsivity of THz QWP device is showing how much photocurrent can be generated by certain amounts of incoming photons. It can be calculated by [42]:

$$R(\lambda) = \frac{I_{photo}}{h\nu\phi} = \frac{e}{h\upsilon}\eta(\lambda)g_{photo} \quad (2.29)$$

where I_{photo} is the measured photocurrent and $\eta(\lambda)$ is the spectral absorption strength. Since I_{photo} is independent of number of modules N, device responsivity R is also not related to the value of N.

Given $p_e \approx 1$ in bound-to-quasibound(or continuum) device, we can calculate the capture probability p_c based on measured device responsivity [42]:

$$p_c = \frac{e}{h\nu}\eta\frac{1}{NR} \tag{2.30}$$

2.2.4 Detectivity

Detectivity is another factor that indicates performance of THz QWP. Compared with responsivity, it also includes the information of device's dark current. Detectivity is generally defined as [42]:

$$D^* = R\sqrt{\frac{A}{S}} \tag{2.31}$$

where R is responsivity, A is device surface area and $S = 4egI_{dark}$ represents dark current power spectral density, assuming $g \approx g_{photo}$.

Because the mechanism of device dark current is different depending on operating temperature, the detectivity is calculated differently at a high or low temperature regime.

At a high temperature, since the dark current mainly comes from thermal activation of the electrons on the ground state, detectivity can be approximated by the 2D or 3D carrier density in the continuum [42]:

$$D_{det}^{*} = \frac{\lambda}{2hc}\frac{\eta}{\sqrt{N}}\sqrt{\frac{\tau_c}{N_{3D}^{ab}L_p}} = \frac{\lambda}{2hc}\frac{\eta}{\sqrt{N}}\sqrt{\frac{\tau_{scatt}}{N_{2D}^{ab}}} \tag{2.32}$$

where τ_c is the capture time, τ_{scatt} is the scattering time and N_{2D}^{ab} and N_{3D}^{ab} are the 2D or 3D carrier density (where $\frac{N_{3D}^{ab}}{N_{2D}^{ab}} = \frac{m_b}{m_e}\left(\frac{m_b k_B T}{2\pi\hbar^2}\right)^{\frac{1}{2}}$). In THz QWP, N_{3D}^{ab} is usually given by [42]:

$$N_{3D}^{ab} = 2\left(\frac{m_w k_B T}{2\pi\hbar^2}\right)^{\frac{3}{2}} \exp\left(-\frac{hc}{\lambda_{cut}k_B T} + \frac{E_f}{k_B T}\right) \tag{2.33}$$

where λ_{cut} is the cut-off frequency and can be approximated by $\lambda_{cut} \approx 1.1\lambda_{peak}$. Therefore, to optimize the detectivity D_{det}^{*}, we have $E_f = 2k_B T$ [42].

At low temperature, the thermal induced dark current becomes smaller than the noise current generated by background photons. Therefore, at this regime, the detector performance is limited by background noise. This temperature regime is then called background limited, or BLIP, regime, and the temperature, below which thermal dark current is smaller than background dark current, is called BLIP temperature, written as T_{BLIP}. T_{BLIP} is given by solving the following equation [42]:

$$\eta_w \tau_c \phi_{back} = 2\left(\frac{m_w k_B T}{2\pi\hbar^2}\right)^{\frac{3}{2}} \exp\left(-\frac{hc}{\lambda_{cut}k_B T} + \frac{E_f}{k_B T}\right) \tag{2.34}$$

where η_w is the absorption strength of single module.

The detectivity can also be written as [42]:

$$D^*_{BLIP} = \frac{\lambda_{peak}}{2hc}\sqrt{\frac{\eta_{peak}}{\phi_{back}}} \quad (2.35)$$

where ϕ_{back} is the background photon flux, η_{peak} and λ_{peak} are the peak absorption strength and wavelength respectively. In order to maximize the T_{BLIP}, the condition that $E_f = k_B T$ needs to be satisfied based on the equations above [42].

2.2.5 Light Coupling Geometries

Due to the absorption selection rule discussed in section 2.1.2, light coupling geometry needs to be intentionally designed to permit intersubband interaction with incoming light.

The 45° facet coupling structure is commonly used in demonstrating the prototype of device thanks to its simplicity. Light is guided into device substrate through a 45° facet and bounces multiple times between top contact layer and bottom surface of substrate. In this case, light can be absorbed each time it goes through the active region, which increases the total absorption. However, this coupling strategy cannot be used in 2D focal plane arrays (FPAs) which requires normal incidence.

Diffraction grating is a typical method for coupling normal incident light into QWIP or THz QWP devices. Unlike 45° facet coupling, this technique requires light to be illuminated from the bottom surface of substrate and usually benefits from a higher absorption efficiency. Thermal imaging application based on diffraction grating geometries has already become commercially available.

Recently, QWIPs or THz QWPs based on other light coupling strategies have been proposed. They are based on different physical phenomenon, such as metamaterials [51], surface plasma [52] and photonic crystals [53]. It has been demonstrated that a patch antenna coupling structure can significantly boost device's temperature performance in mid-infrared region [40]. However, there hasn't been much improvement in THz QWP with patch antenna or similar optical coupling structures.

2.3 Device Simulation

To better predict device performance and generate new THz QWP design, a precise simulation model has been constructed based on commercial software MATLAB. Using this numerical solver, both optical absorption and electrical properties can be analyzed given its quantum well structure and device geometry.

This model is targeting at quantum well photodetectors based on GaAs/$Al_xGa_{1-x}As$ material system that absorbs in terahertz region. Since the intersubband transition only requires very low energy to absorb terahertz light, quantum structure in THz QWPs usually have a low aluminum fraction below 5%. In this case, many body effect will heavily impact conduction band and intersubband transition energy and has been taken into account in the model. In the model, band tilting due to many body effects is solved self-consistently with calculating all the energy states, wavefunctions and carrier distributions.

2.3.1 Potential Calculation

The current photoconductive THz QWPs investigated by this model are all based on single-well symmetric structure. Given all quantum structure parameters, including layer thickness of quantum barrier and well, aluminum fraction and doping density, energy levels and wavefunctions can be obtained by using transfer matrix method. To make the simulation more accurate, effective mass nonparabolicity has been considered by introducing a nonparabolicity coefficient which equals 4.9×10^{-19} m^2. As a result, effective mass of electrons becomes dependent on its energy and position, whether in barrier or well region.

As for many body effects mentioned in section 2.1.3, only static effects, including Hartree potential and exchange-correlation potential, are included in self-consistent calculation. Figure 2.7 presents the conduction band and confined energy levels as a demonstration.

As shown in Figure 2.7, the ground state is well confined while the first excited state is aligned with the top edge of conduction band. In this case, the first excited state is only 4meV lower than the energy of barrier. For typical QWIP or THz QWP structures, dopants locate at the center of a quantum well leading to downward bending and a deeper well. This many body effect will result in a higher energy separation than designed value and poorer alignment between the first excited state and barrier edge. Therefore, it is necessary to include the many body effect especially when designing THz QWPs.

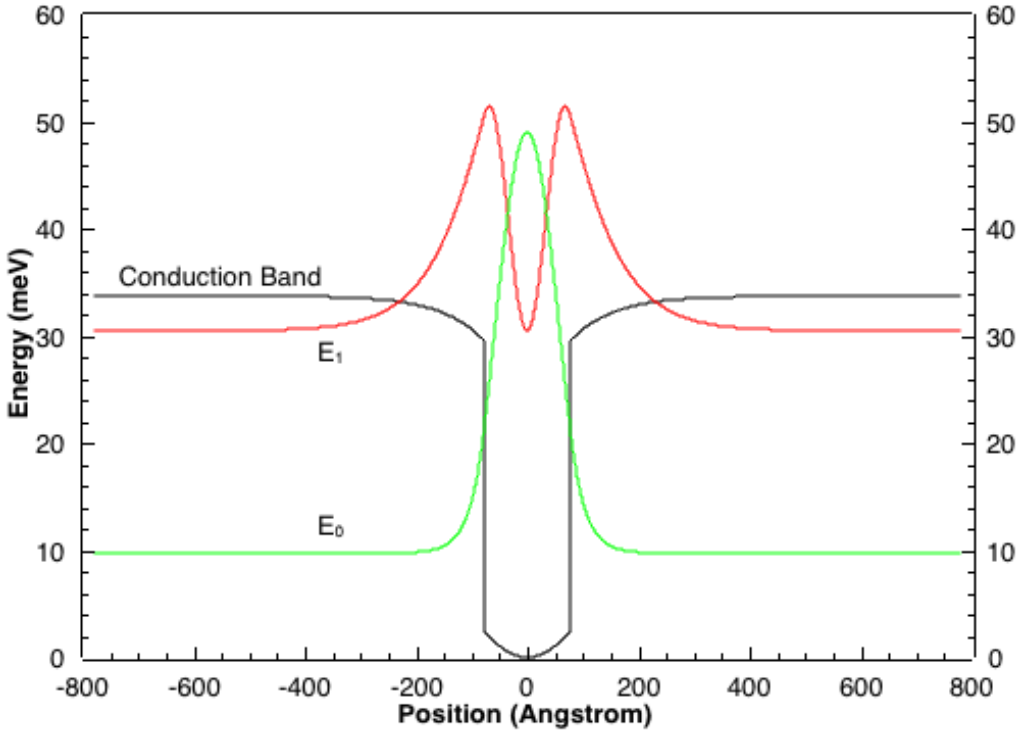

Figure 2.7 Simulated (using developed MATLAB model) conduction band and confined energy levels in THz QWP (V266, structure parameters extracted from [54]*, see Table 2.1)*

2.3.2 Absorption Spectrum Simulation

Absorption strength can be calculated based on (2.9) and the potential profile given by the previous section. To get the real absorption energy, dynamic many body effects need to be taken into consideration. There are two main dynamic factors, depolarization and exciton-like shift. However, exciton-like shift is mostly overestimated in THz QWP [44], and it is common to simply leave out its contribution and only consider depolarization shift. In this case, intersubband transition resonant energy in (2.14) is then expressed as [42]:

$$\tilde{E}_{21}^2 = E_{21}^2(1+\alpha) \tag{2.36}$$

Following table (Table 2.1) gives the structure of some published THz QWP devices.

Sample	L_w (nm)	L_b (nm)	Al (%)	N_{3D} (cm^{-3})	N_{2D} (cm^{-2})	Number of Modules
A0175	155	702	3	1.5×10^{-17}	1.5×10^{-11}	30
V266	155	702	3	6×10^{-16}	6×10^{-10}	30
V267	221	951	1.5	3×10^{-16}	3×10^{-10}	23

Table 2.1 Structure parameters of A0175 [44], *V266 and V267* [54]

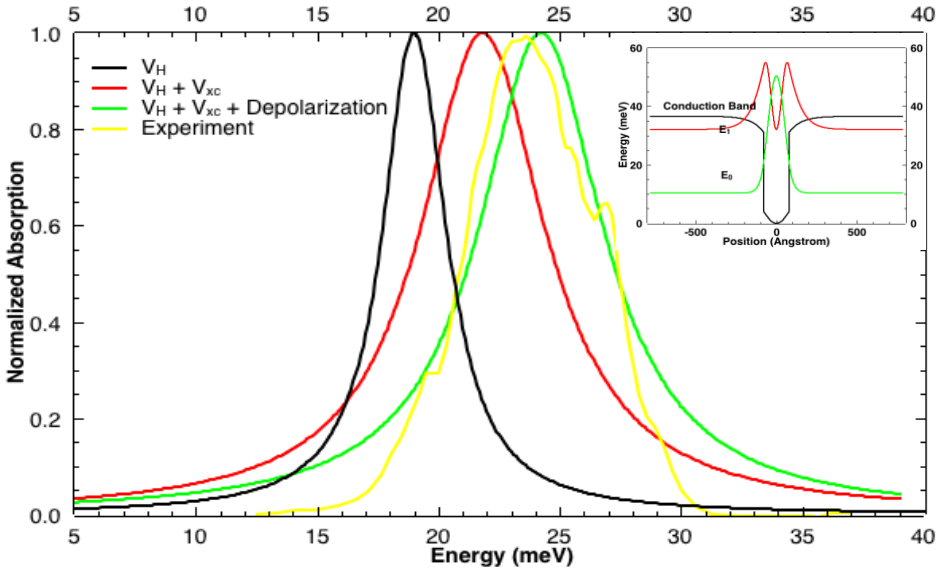

Figure 2.8 Simulation (calculated using developed MATLAB model) and experiment results(extracted from [44]*) of absorption spectrum (A0175) including many body effects; inset: simulated band diagram and wavefunctions of A0175*

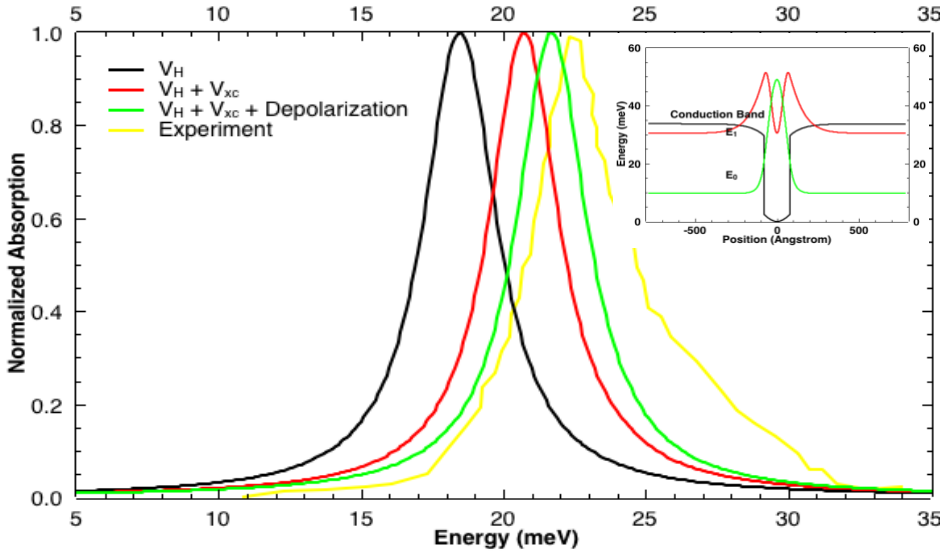

Figure 2.9 Simulation (calculated using developed MATLAB model) and experiment results (extracted from [54]*) of absorption spectrum (V266) including many body effects; inset: simulated band diagram and wavefunctions of V266*

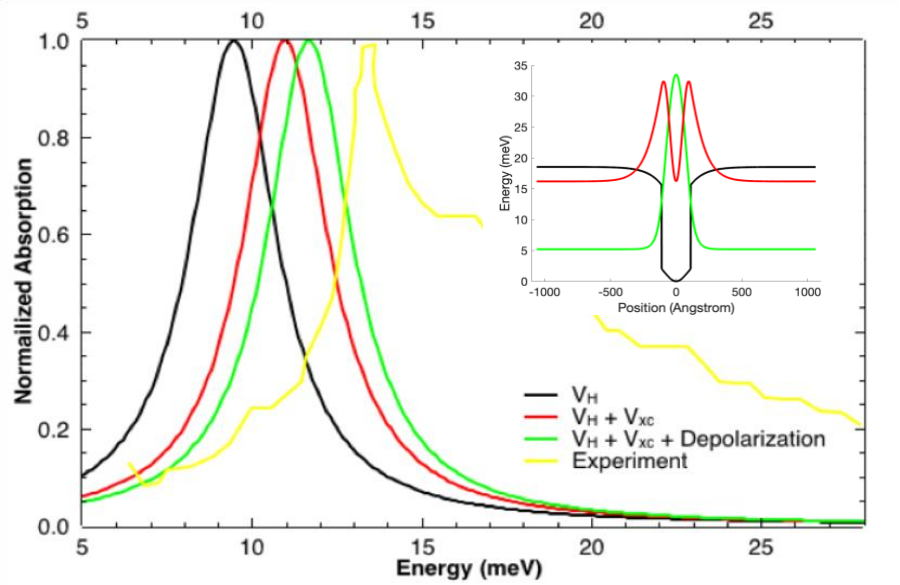

Figure 2.10 Simulation (calculated using developed MATLAB model) and experiment results (extracted from [54]*) of absorption spectrum (V267) including many body effects; inset: simulated band diagram and wavefunctions of V267*

As shown in Figure 2.8, Figure 2.9 and Figure 2.10, by including Hartree potential, exchange-correlation potential and depolarization effect in the simulation model, absorption spectrum gradually shifts closer to experiment result. From the figure, we can conclude that exchange-correlation plays the most important role in causing the difference. The inconsistency between simulation and experiment becomes more dramatically as doping density drops, which indicates that, at lower doping, exchange-correlation potential may be underestimated by the approximation in (2.13).

2.3.3 Dark Current Simulation

In the simulation model, dark current is estimated by transmission probability model. This model takes account of direct interwell tunneling, thermionic emission and thermal assisted tunneling. To better calculate the real dark current, electron drift mobility is extracted from published results [50] as a temperature-dependent parameter to fit the dark current amplitude is this model (shown in Figure 2.11). Validation of the dark current model has been carried out by comparing the simulation results with published experiment data for device V267 [50] and L924 [55] from different groups.

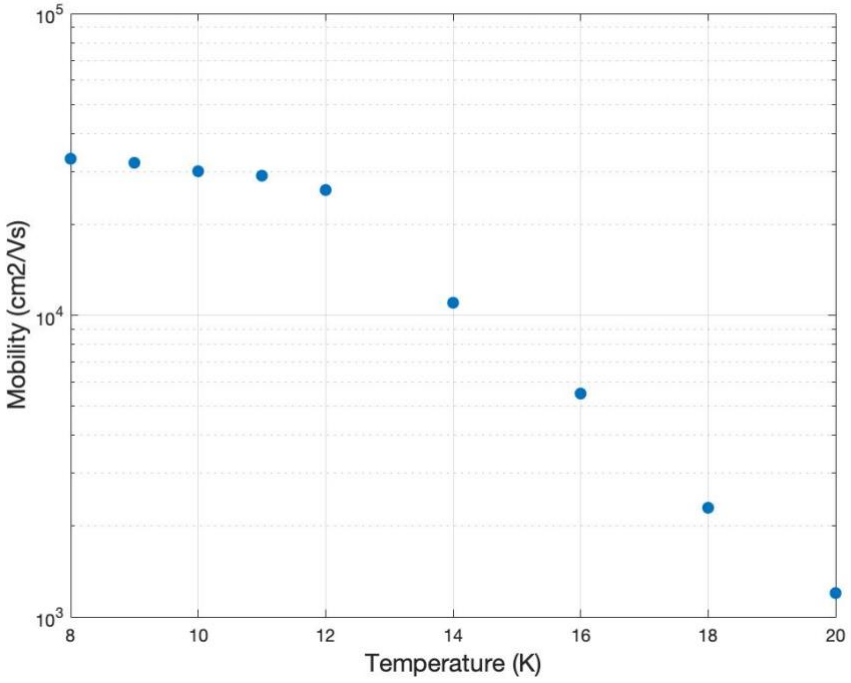

Figure 2.11 Extract drift mobilities as a function of temperature from [50]

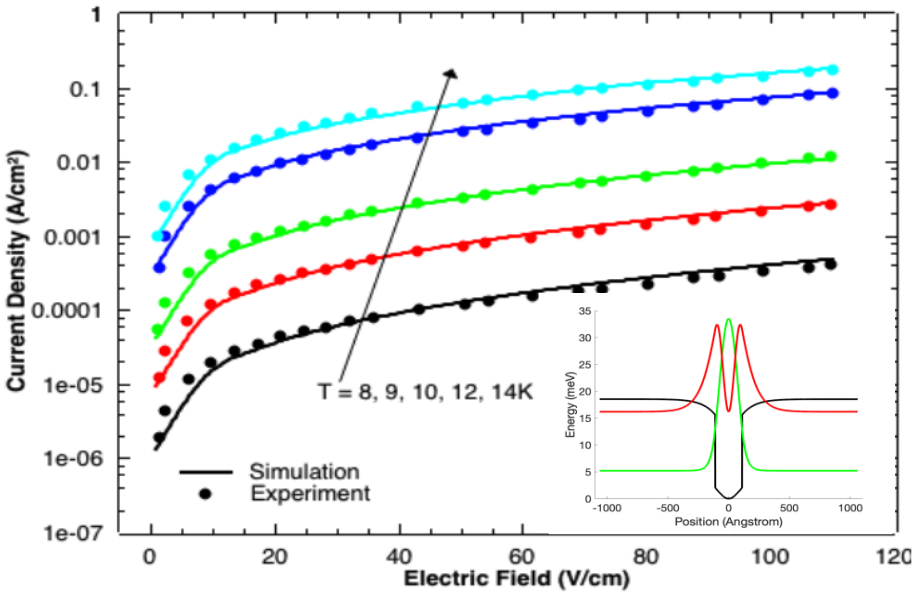

Figure 2.12 Simulation (calculated using developed MATLAB model) and experiment results (extracted from [50]*) of dark current (V267) based on transmission coefficient model; inset: simulated band diagram and wavefunctions of V267*

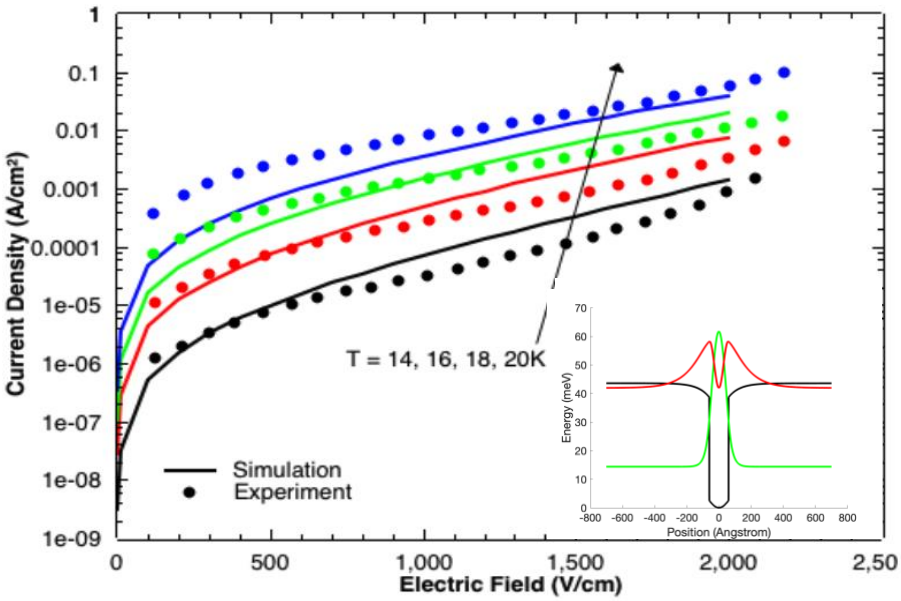

Figure 2.13 Simulation (calculated using developed MATLAB model) and experiment results (extracted from [55]*) of dark current (L924) based on transmission coefficient model; inset: simulated band diagram and wavefunctions of L924*

Figure 2.12 and Figure 2.13 show the temperature-dependent dark current density for V267 and L924. Simulation results and experiment data agree with each other very well in V267 and remain at the same magnitude in L924, even though simulation becomes slightly off in L924 as temperature raises. From the figures, it can also be concluded that at higher temperature region, the simulated dark current density is more underestimated which may result from underestimation of thermionic dark current.

2.4 Electric Characterization

This section reports the characterization setup and result for device G0219. THz QWP G0219 is grown by Alan Tam in the MBE laboratory held by Prof. Zbig Wasilewski at the University of Waterloo. Its active region contains 23 periods and each of them is composed of a 95.1 nm $Al_{0.015}Ga_{0.985}As$ quantum barrier and a 15.7 nm GaAs quantum well. The center 10 nm of quantum well region is doped with silicon with a sheet density of 4×10^{-10} cm^{-3}.

The thicknesses of AlGaAs and GaAs, as well as the aluminum fraction, are determined by engineering the energy bands so that the energy levels separation is close to desired absorption wavelength. Doping level is determined by (2.3) and (2.4) to maximize device temperature performance. The number of periods and doping position are kept same as V267 (shown in Table 2.1). This structure has a bound-to-quasibound transition and, considering many body effects, has a simulated absorption wavelength around 100 μm.

Device fabrication is done with the help of Dr. Chao Xu in Quantum NanoFab at the University of Waterloo. Device mesa (active region area) is sandwiched by Si-doped GaAs contact layers and fabricated by wet etching. Both top and bottom contact metal layers consist of Ni/Ge/Au, which are annealed after deposition to form Ohmic contacts.

Afterwards, device is lapped with 45° facet on the substrate as light coupler and mounted on a homemade oxygen-free copper package which is coated with gold layer. The growth sheet and fabrication process of G0219 can be found in Appendices.

2.4.1 j-V Characteristics and BLIP temperature

Device is carefully cleaved into multiple bars and lapped with a 45° side facet. On each bar, there are devices with different mesa sizes fabricated. Mesas are in square shape and their rims are 200 μm, 400 μm, 600 μm, 800 μm and 1 mm. Figure 2.14 illustrates the top view of cleaved device bar together with all the devices in different mesa sizes.

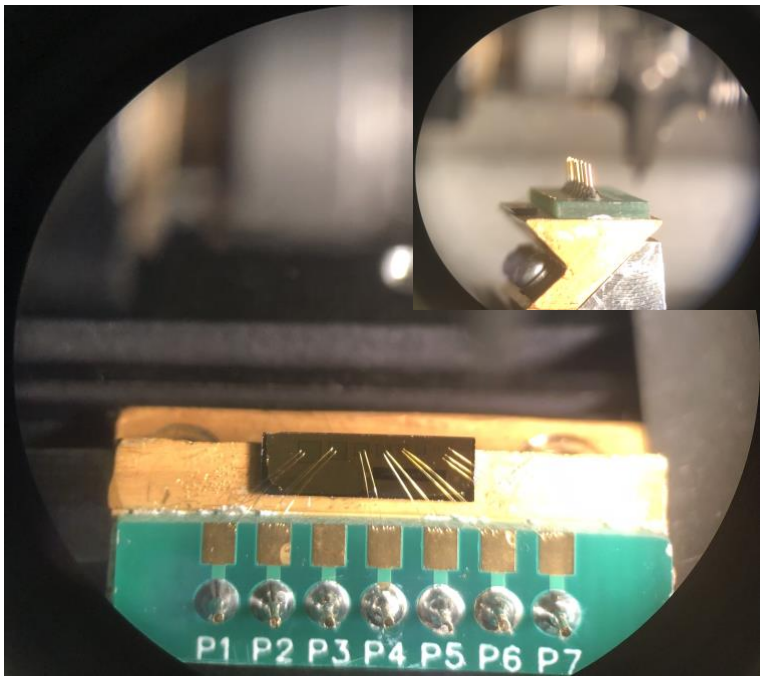

Figure 2.14 Top view of the device mounted on a package (squares in dark gold color are the top contacts for different device mesas; and surrounding gold is the common bottom contact). Inset: sideview of the device and package showing the 45 degree facet

A cleaved device bar is mounted on a home-made copper package, where incoming light can be coupled into device substrate perpendicularly, and then attached to the cold finger of a cryostat system. Cryostat under high vacuum can be continuously cooled down to 8 K and stable at any

temperature setpoint ranging from 8 K to room temperature by applying a heater inside cryostat chamber.

To characterize current density-voltage (j-V) performance, each device is connected by BNC cable inside the cryostat and biased through a Keithley SourceMeter. Dark condition is achieved by an aluminum shield fully covering the device and cold finger from room-temperature background radiation. The experiment setup is illustrated in Figure 2.15.

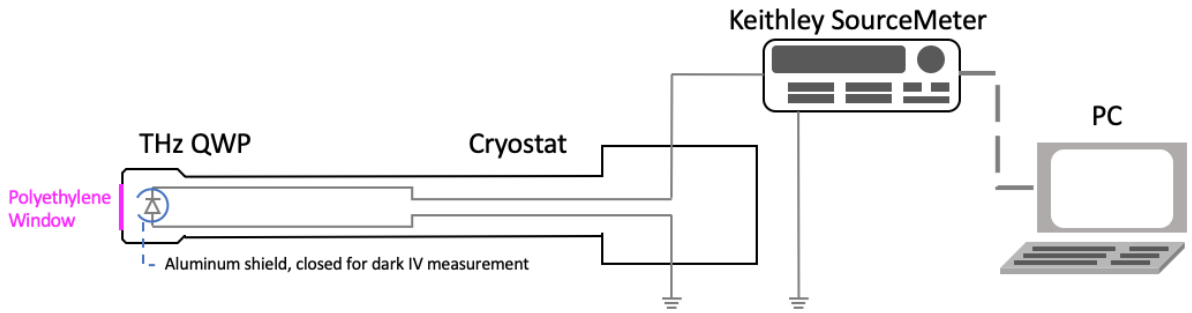

Figure 2.15 Experiment setup of IV characterization

As shown in Figure 2.15, there is a small opening on aluminum shield, which is used to measure background IV curve of the device that locates at the center of the opening.

Figure 2.16 and Figure 2.17 report device dark and background j-V curves as a function of applied bias, under temperatures ranging from 8 K (9 K for background j-V) to 16 K. Since, at 8 K, cryostat is reaching its limit of lowest cooling temperature, introducing background radiation will lead to a higher stabilized temperature with full cooling power. Figure 2.18 shows the measured ratio between I_{back} and I_{dark} as a function of applied bias under different temperature. As defined in chapter 2, ratio I_{back}/I_{dark} equals 2 as device is under BLIP condition, which

means that the photocurrent noise generated by background radiation is the same as the device dark current.

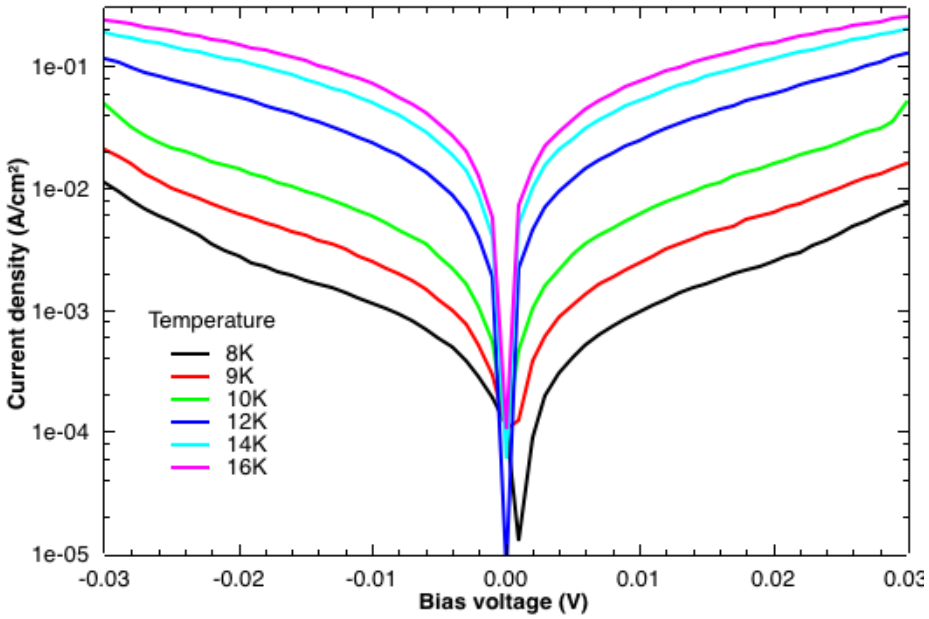

Figure 2.16 Measured dark current density of G0219 (device size: 600 µm) from 8 K to 16 K

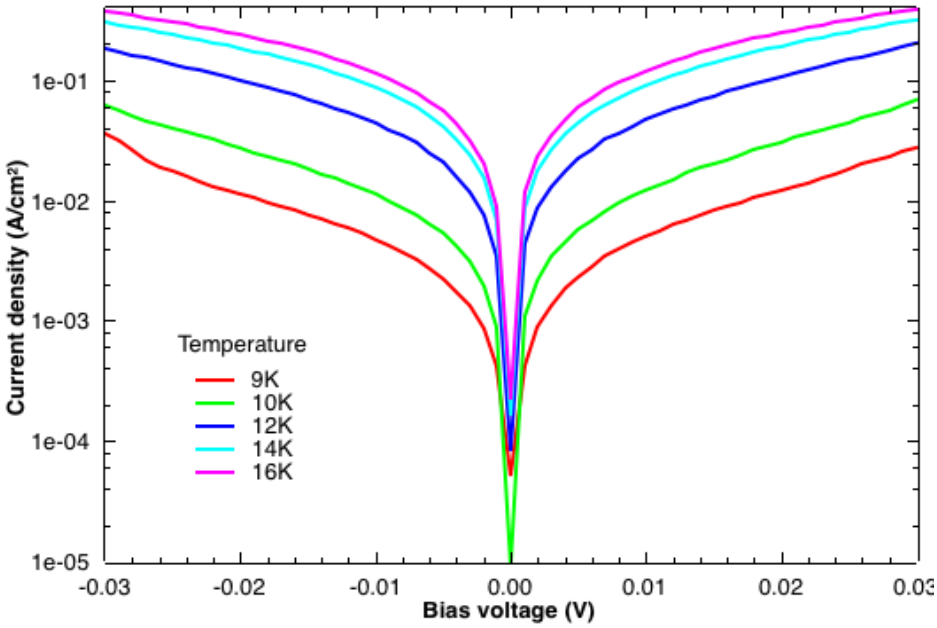

Figure 2.17 Measured background current density of G0219 (device size: 600 µm) from 9 K to 16 K

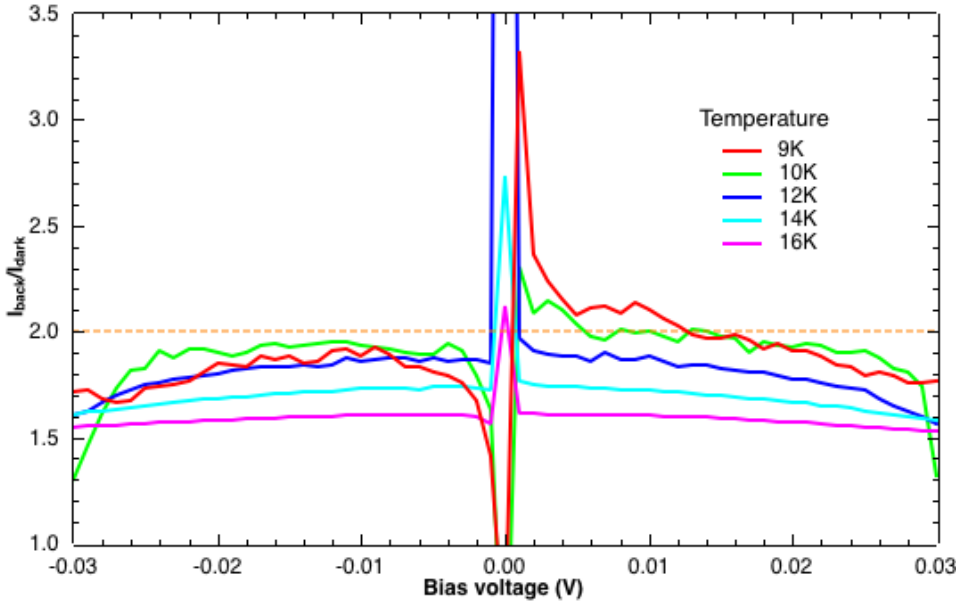

Figure 2.18 Ratio between background and dark current density as a function of bias voltage of G0219 (device size: 600 μm) from 9 K to 16 K

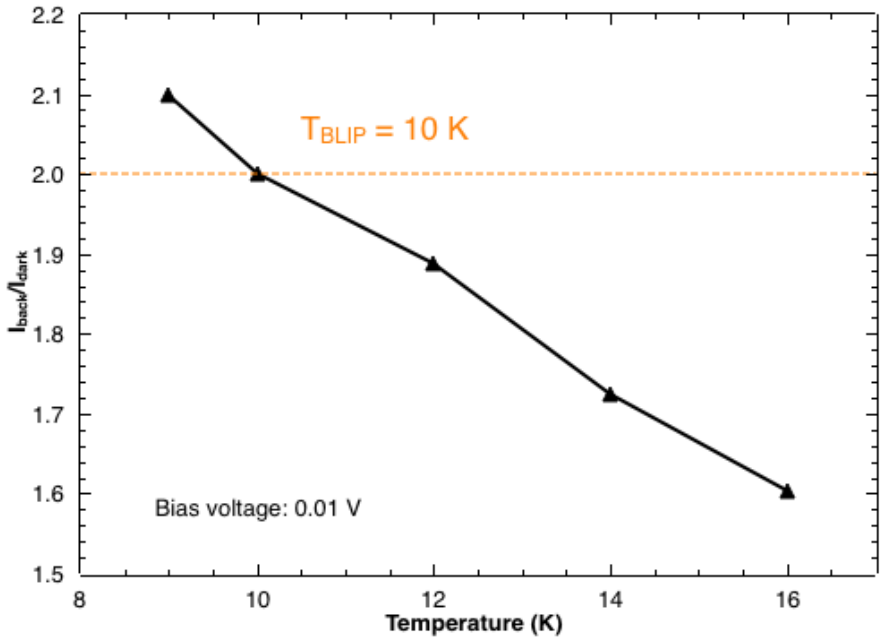

Figure 2.19 Ratio between background and dark current density as a function of temperature (device size: 600 μm). Calculated BLIP temperature of G0219 is 10 K

As Figure 2.16 and Figure 2.17 present, dark current and background current density dramatically increase with temperature below 20 K. At lower temperature from 8 K to 12 K, measured current density is sensitive with device temperature; whereas it becomes stabilized as temperature goes above 14 K. It can also be concluded that dark current and background current are symmetric with respect to bias voltage, which agrees with typical behavior of photoconductive THz QWP. In Figure 2.16, minimum dark current appears at non-zero bias when temperature is 8 K. This shift is contributed by dopant segregation in quantum well region during growth process and is classical in the context of QWIPs and THz QWPs, as presented in [42] and [56].

Figure 2.18 shows the ratio I_{back}/I_{dark} as a function of bias voltage at different device temperature. Dotted line indicates the BLIP condition when the ratio I_{back}/I_{dark} equals 2. As the temperature and absolute value of bias increases, I_{back}/I_{dark} gradually drops. Figure 2.19 clearly presents the ratio I_{back}/I_{dark} decreasing with temperature under a bias voltage of 0.01 V, and device BLIP temperature is 10 K.

Measured dark current is then compared with the simulation model by setting electron drifting mobility as the fitting parameter. As shown in Figure 2.20, simulated dark current density curves are well aligned with measurement results at temperature above 9 K. Values of electron drifting mobility is based on Figure 2.11. At 8 K, simulated dark current is lower than measured results by one order of magnitude, which may due to the fact that measurement system is close to its cooling limit and device temperature may not be stale and uniform during characterization

process. In addition, any unwanted background radiation will make a difference since the current density is already very low at 8 K.

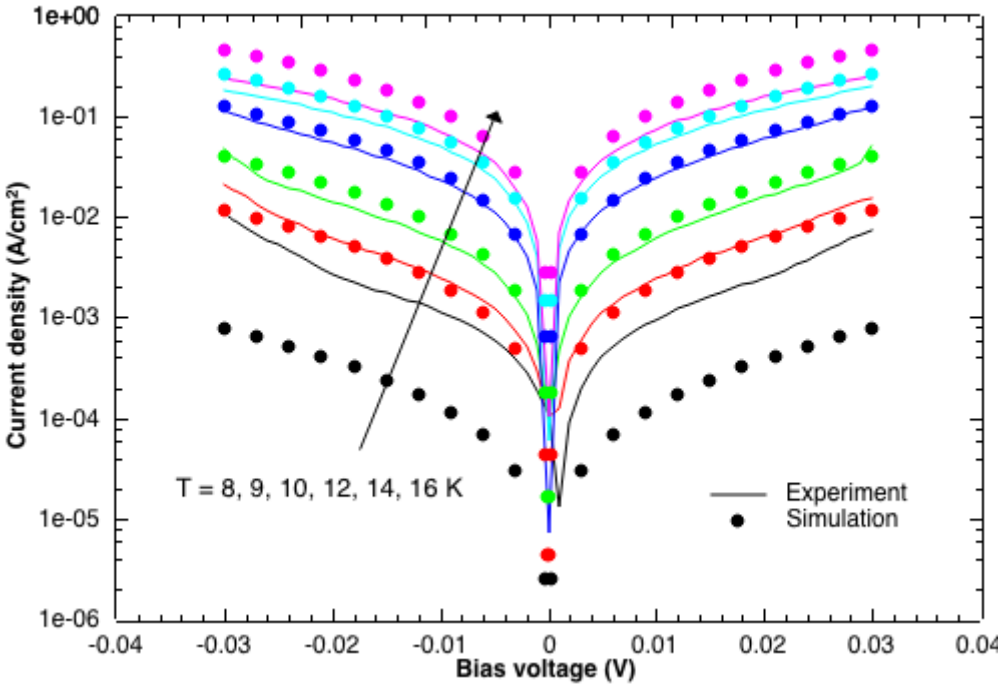

Figure 2.20 Comparison between simulation and measured dark current density as a function of bias for G0219 (device size: 600 μm)

Impact ionization is observed by further increasing bias voltage up to ±40 mV. In THz QWP, it is due to the free carriers that injected from metal contacts. At higher bias, the first few quantum wells are depleted so that more and more carriers flow from metal contact into active region to compensate for the carrier loss and lead to a barrier breakdown. The impact ionization has also been reported [57]. This phenomenon is demonstrated by Figure 2.21, which presents the measured current density as a function of bias voltage from 8 K to 12 K in log scale. As it shows, there is a dramatic change in slope when the absolute value of bias voltage is higher than 30mV at low temperature. Current density difference at breakdown voltage reduce with the temperature

and finally disappear at 12 K. As bias is close to ±40 mV, the current increase starts to slow down and becomes saturated at same level even under different temperatures. This behavior can be attributed to the fact that both high temperature and high bias can increase the number of electrons in the continuum, which will saturate as there are not much electrons left inside quantum wells. The asymmetry, similar as Figure 2.16, is due to the segregation of aluminum and silicon in active region. The multi-step behavior observed merely at negative bias near breakdown voltage probably results from the breakdown at different quantum wells, which needs further research.

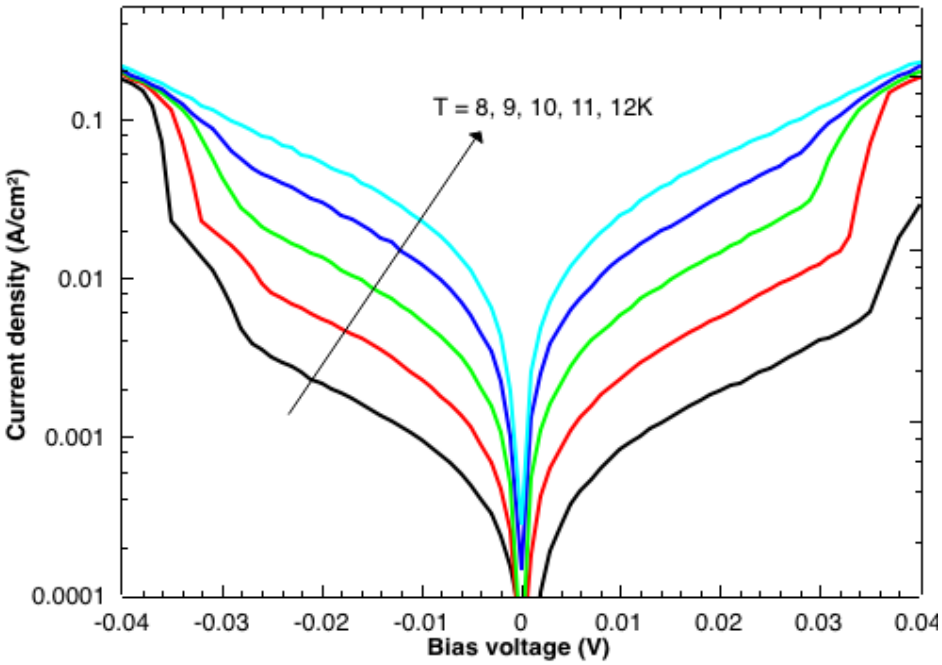

Figure 2.21 Current density as a function of bias voltage of G0219 (device size: 600 μm). Barrier breakdown observed under ±32 mV at 8, 9 and 10 K

Effect of sidewall leakage on device dark current is also investigated. In ideal case, THz QWP will have a consistent dark current density regardless of device size. However, leakage current through mesa sidewall can contribute to measured dark current and, as a result, lower device

performance. Unlike real dark current, sidewall leakage current is proportional to the length of mesa and will lead to higher dark current density for device with smaller area.

The dark current density curves of devices with different mesa size are plotted out in the following figures. The mesa lengths of measured devices are 1 mm, 800 µm, 600 µm and 400 µm respectively; and two devices are both in 600 µm for comparison.

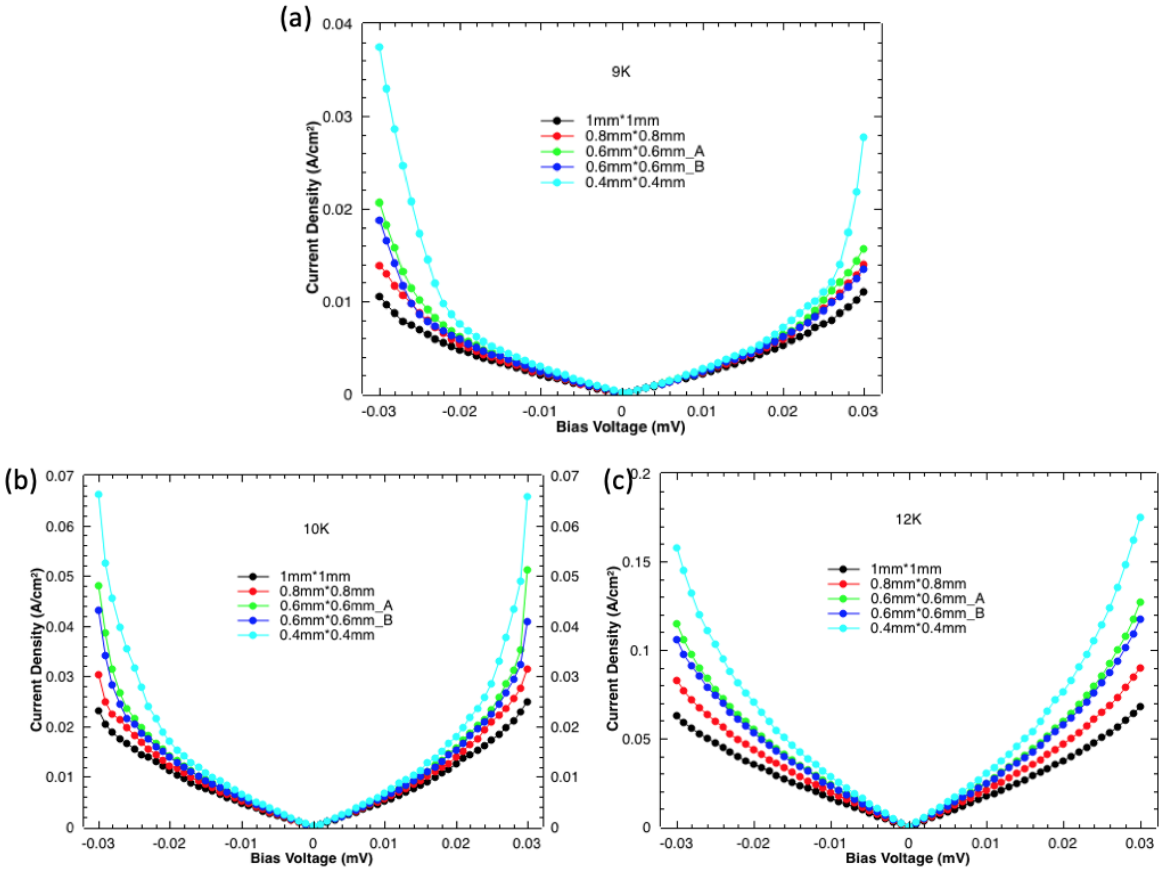

Figure 2.22 Measured dark current density as a function of bias for devices with different mesa sizes at (a) 9 K, (b) 10 K and (c) 12 K

It is clearly shown from Figure 2.22 that measured dark current density under same bias voltage is changing with device mesa size at same temperature. Devices with smaller mesa size corresponds to higher dark current density. As is known, sidewall leakage current is proportional

to sidewall surface area, which is in linear with mesa length. Therefore, measured dark current density, which equals measured dark current divided by mesa area, will be in reverse linear with mesa length if sidewall leakage current exists. Moreover, the two devices with same mesa size shows similar current density compared with others. As a result, the difference in dark current density among all the devices can be attribute to sidewall leakage.

As the figures show, leakage current remains moderate at lower bias voltage whereas it becomes significant under impact ionization region. When temperature goes higher than 12 K, impact ionization behavior is no longer observable, thus leakage current smoothly increases within operating bias. Furthermore, at 12 K, there is a distinct difference among measured dark current density curves compared with lower temperature. This phenomenon is probably due to a higher surface recombination rate at higher temperatures and needs to be further investigated.

2.4.2 Absorption Spectrum

Device spectrum is measured with ThermoFisher Nicolet is50 Fourier-transform Infrared Spectroscopy (FTIR) when cooled down to 7.7 K. Measurement setup is illustrated by Figure 2.23. As it shows, device is biased via current pre-amplifier and the amplified photocurrent signal plus background noise is then feed to the detector interface of the FTIR. Infrared light from internal IR source is focused onto detector by terahertz lens to maximize signal to input power and signal to noise ratio.

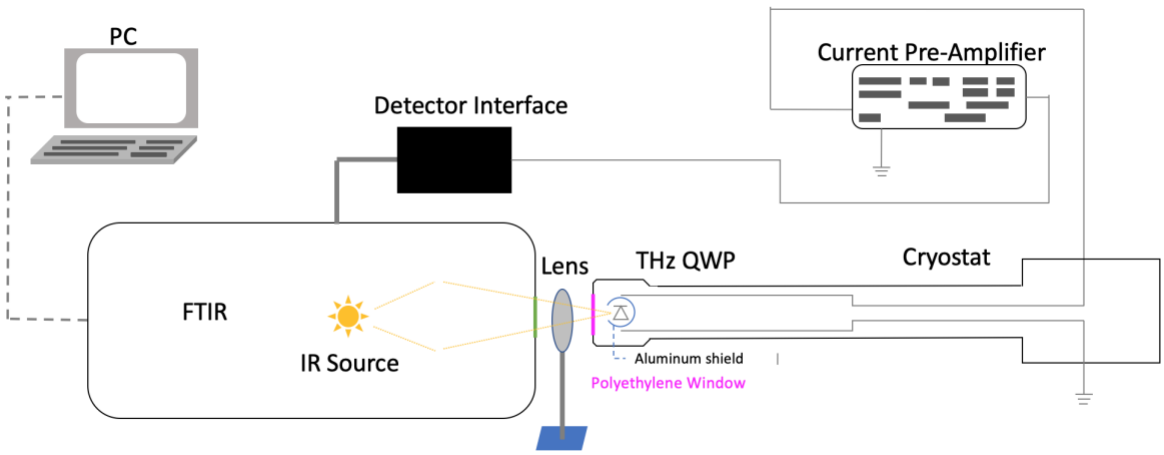

Figure 2.23 Experiment setup of spectrum measurement

Spectrum scanning time is set to be long enough to minimize noise level and eliminate the fluctuation in measured spectrum. Figure 2.24 reports the measured spectrum for device with mesa length of 600 μm under 25 mV at 7.7 K.

According to Figure 2.24, after subtracting background noise and source emission spectrum, real absorption happens between 94.5 cm^{-1} (2.83 THz) and 141.7 cm^{-1} (4.25 THz) wavenumber. Peak absorption is achieved at 107.32 cm^{-1} (3.22 THz), whereas it shows relatively flat absorption rather than a sharp peak within absorption range. The calculated absorption bandwidth is therefore 1.42 THz. It also worth noting that absorption peak shows different slope at its two sides. Absorption sharply increases at lower wavenumber end but slowly decreases at higher wavenumber end, which reaches zero absorption at 200 cm^{-1} (6 THz) wavenumber. This behavior can further prove the absorption is achieved by bound-to-continuum transition.

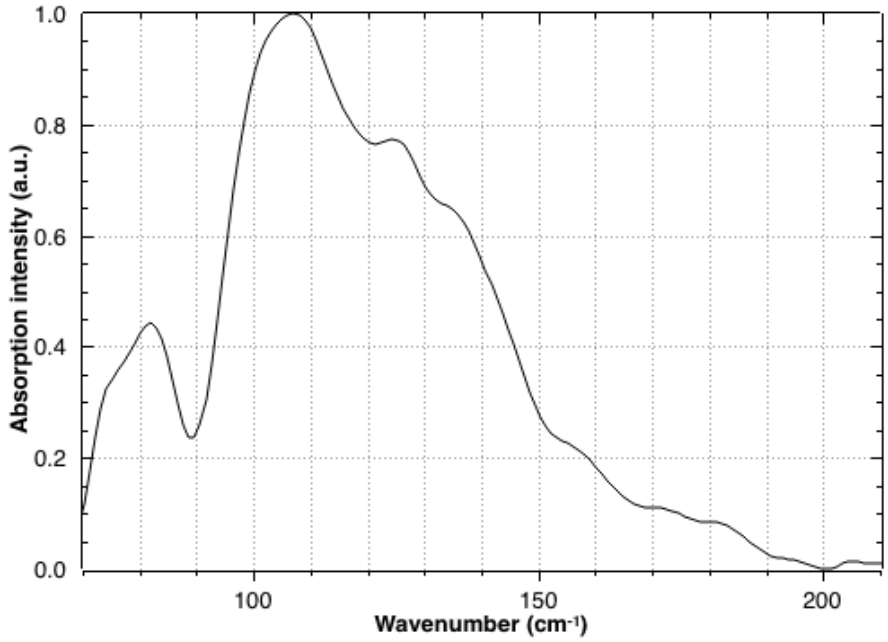

Figure 2.24 Normalized spectrum of G0219 (device size: 600 μm) measured under 25 mV at 7.7 K. Peak response at 107.32 cm^{-1}

2.4.3 Responsivity

As previously defined in section 2.2.3, responsivity is the ratio between generated photocurrent I_{photo} and corresponding incident power P_{in} seen by the detector. To measure device responsivity, the incident power is supplied by a calibrated blackbody radiator at 1173 K. The experiment setup is illustrated in Figure 2.25. Infrared Systems M-67030 Blackbody Reference Source is used as the light source, on which there is an aperture wheel to adjust the beam size.

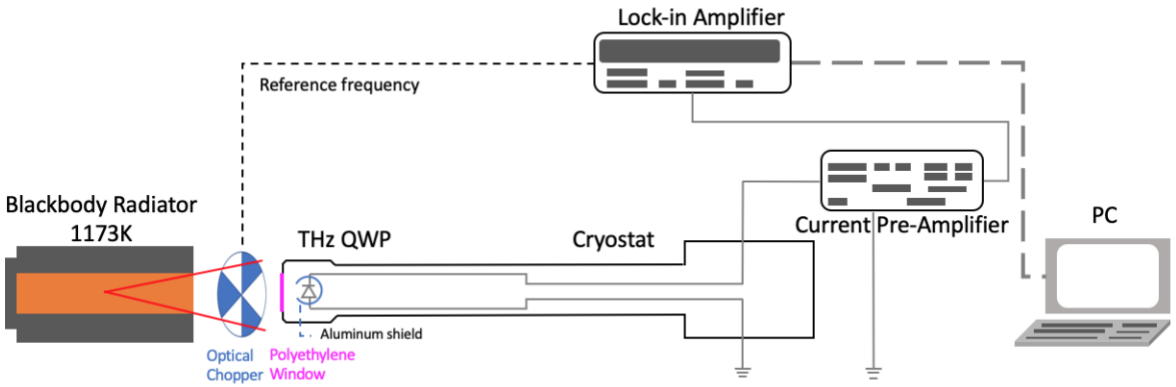

Figure 2.25 Experiment setup of responsivity characterization

The outcoming beam is modulated by an optical chopper at a reference frequency of 400 Hz and penetrates through the polyethylene window before shining onto detection surface. The detector, as measuring the background photocurrent noise, is covered by an cold aluminum shield with small opening. A SR570 current preamplifier applies the bias voltage onto the device and amplifies the total photocurrent, which includes the dark current and background noise as well. To filter out these noise current, the amplified current is then injected into a lock-in amplifier which extract only the signal from excited photocurrent plus the noise at reference frequency.

Figure 2.26 shows the calculated photocurrent as a function of applied bias and operating temperature.

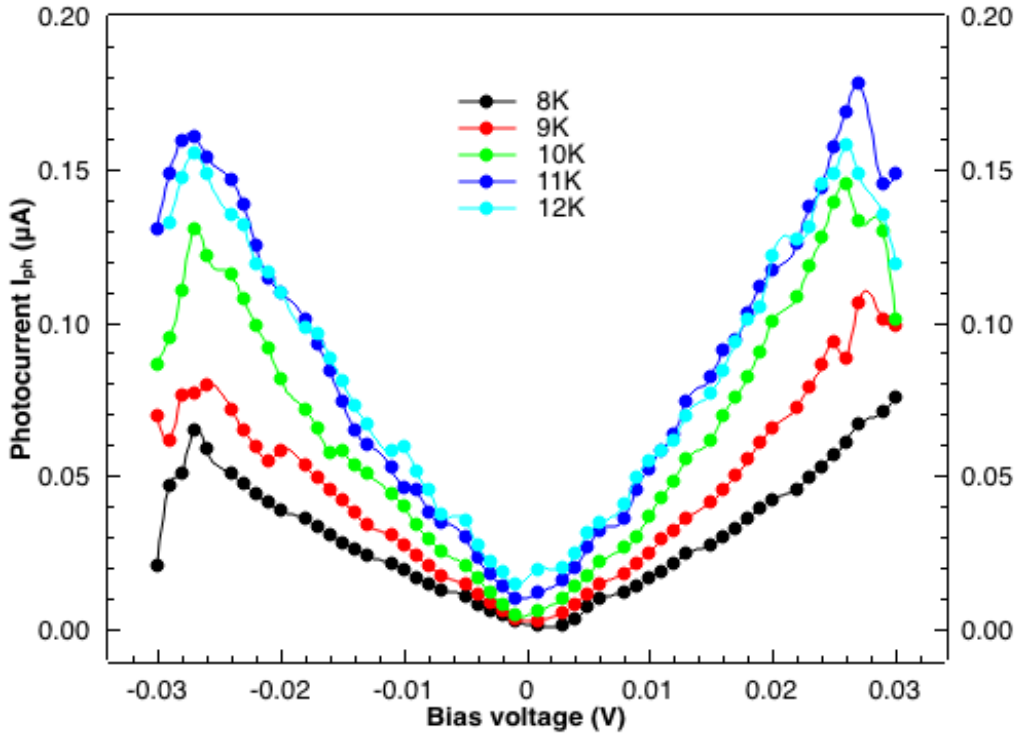

Figure 2.26 Calculated photocurrent of G0219 (device size: 600 μm) from 9 K to 12 K as a function of bias voltage under 1173 K blackbody radiation

As it reveals, photocurrent generally follows a linear relation with applied bias, which agrees with the typical behavior in bound-to-continuum intersubband transition. Increasing device temperature, up to 11 K, will result in more photocurrent being generated; however, operating at 12 K can lead to poorer performance, especially at higher bias. Photocurrent eventually vanishes when further increasing temperature to 14 K. Highest photocurrent is achieved at 11 K under bias voltage of 26 mV. Similar to j-V characterization, asymmetry is observed and may be due to dopant segregation.

To characterize real peak responsivity, it is necessary to estimate input power by applying the Planck's law to the blackbody radiator. In blackbody, spectral radiant emittance W_λ can be calculated by

$$W_\lambda = \frac{C_1}{\lambda^5 \left(e^{\frac{C_2}{\lambda T}} - 1 \right)} \tag{2.37}$$

where $C_1 = 3.7415 \times 10^4$ W · μm^4/cm^2 and $C_2 = 1.43879 \times 10^4$ μm^4 · K. λ is wavelength in microns and T is temperature in Kelvin. Spectral infrared irradiance can then be determined by

$$H_\lambda = W_\lambda t(\lambda) \frac{a^2}{4d^2} \tag{2.38}$$

where W_λ is radiant emittance of the infrared source, t is transmission of the optical path, a is the limiting aperture diameter and d is distance from the aperture plane to the sensing area plane.

Figure 2.28 shows the real peak responsivity calibrated based on the experiment setup, in which case $a = 1.5$ cm and $a = 5$ cm. The spectral transmission of polyethylene window is considered as the $t(\lambda)$ and measured by the FTIR. Moreover, the spectral responsivity can be represented as

$$R(\lambda) = R_{peak} \xi(\lambda) \tag{2.39}$$

Where $\xi(\lambda)$ is the measured absorption spectrum normalized to the peak value of absorption and R_{peak} is the peak responsivity. Therefore, we have

$$I_{ph} = \int_{\lambda_1}^{\lambda_2} R(\lambda) P(\lambda) d\lambda = R_{peak} \int_{\lambda_1}^{\lambda_2} \xi(\lambda) P(\lambda) d\lambda = R_{peak} \frac{a^2}{4d^2} A_{det} \int_{\lambda_1}^{\lambda_2} \xi(\lambda) W_\lambda t(\lambda) d\lambda \tag{2.40}$$

$$P_{in} = \frac{a^2}{4d^2} A_{det} \int_{\lambda_1}^{\lambda_2} \xi(\lambda) W_\lambda t(\lambda) d\lambda \tag{2.41}$$

Where A_{det} is the detection area (2.55×10^{-3} cm^2) and P_{in} is the total power that responded by the photodetector. Given $t(\lambda)$, $\xi(\lambda)$ and the parameters mentioned above, the integral can be

calculated. The spectrum of $\xi(\lambda)W_\lambda t(\lambda)$ is shown in Figure 2.27. According to the calculation, P_{in} is 9.39×10^{-8} W.

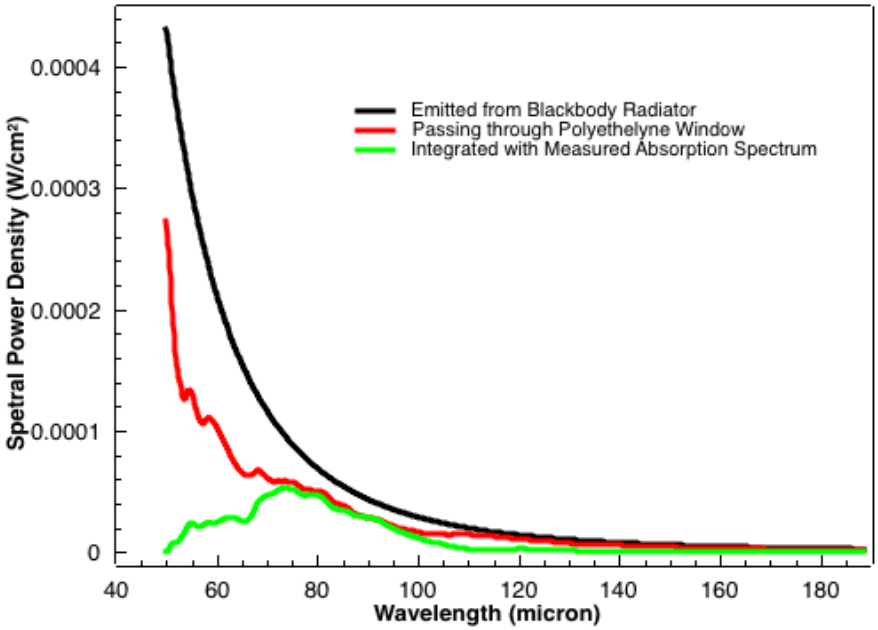

Figure 2.27 Spectral power density for different cases

Therefore, peak responsivity can be given by dividing photocurrent I_{ph} by total power P_{in}. Calibrated peak responsivity is shown in Figure 2.28.

Responsivity curves show the same trends with generated photocurrent. It reaches the highest value, 1.9 A/W, at 11 K under both 26 mV. Higher electric field across the active region will cause the misalignment of excited energy subband with the top barrier edge and reduce its responsivity.

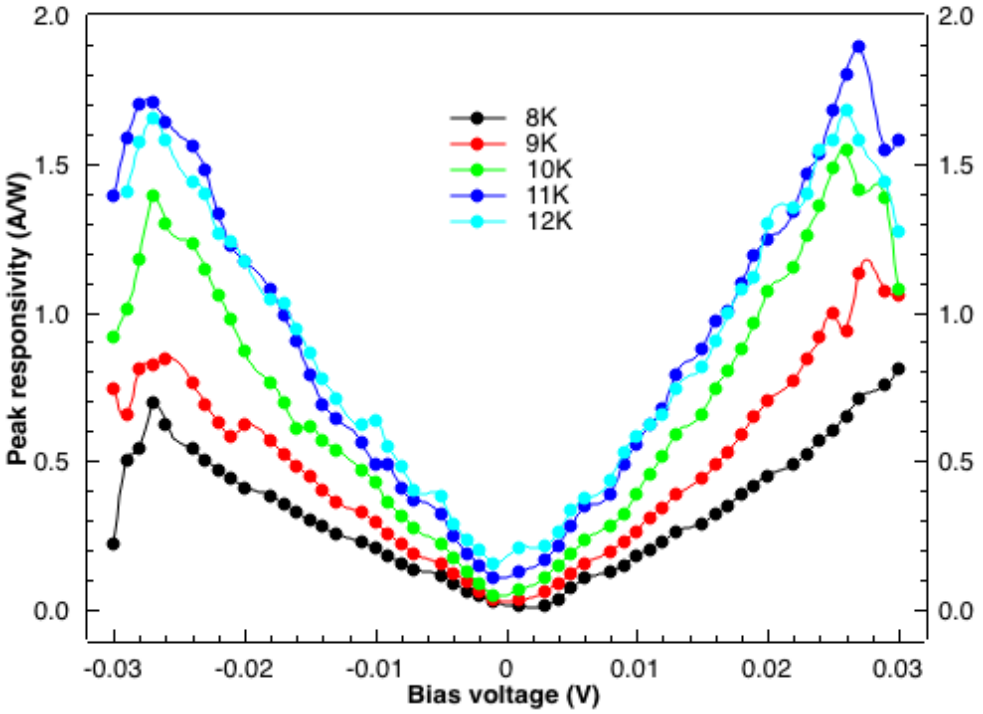

Figure 2.28 Calculated responsivity of G0219 (device size: 600 μm) from 9 K to 12 K

2.4.4 Detectivity

Detectivity is an evaluation on device performance in the perspective of both generating photocurrent signal and suppressing dominating dark noise. To calculate detectivity, it is necessary to extract photoconductive gain from measured responsivity by (2.29). In this equation, values of absorption strength and intersubband transition energy are given by simulation, shown in Table 2.2. Detectivity is then evaluated by (2.31) and presented in Figure 2.29. g_{photo} and $S = 4egI_{dark}$ are given by measurement results of device responsivity and dark current density.

Parameters	ν (THz)	η_{peak}	A (cm^2)
Values	2.9	0.0111	2.55×10^{-3}

Table 2.2 Simulated parameters used to calculate detectivity of G0219

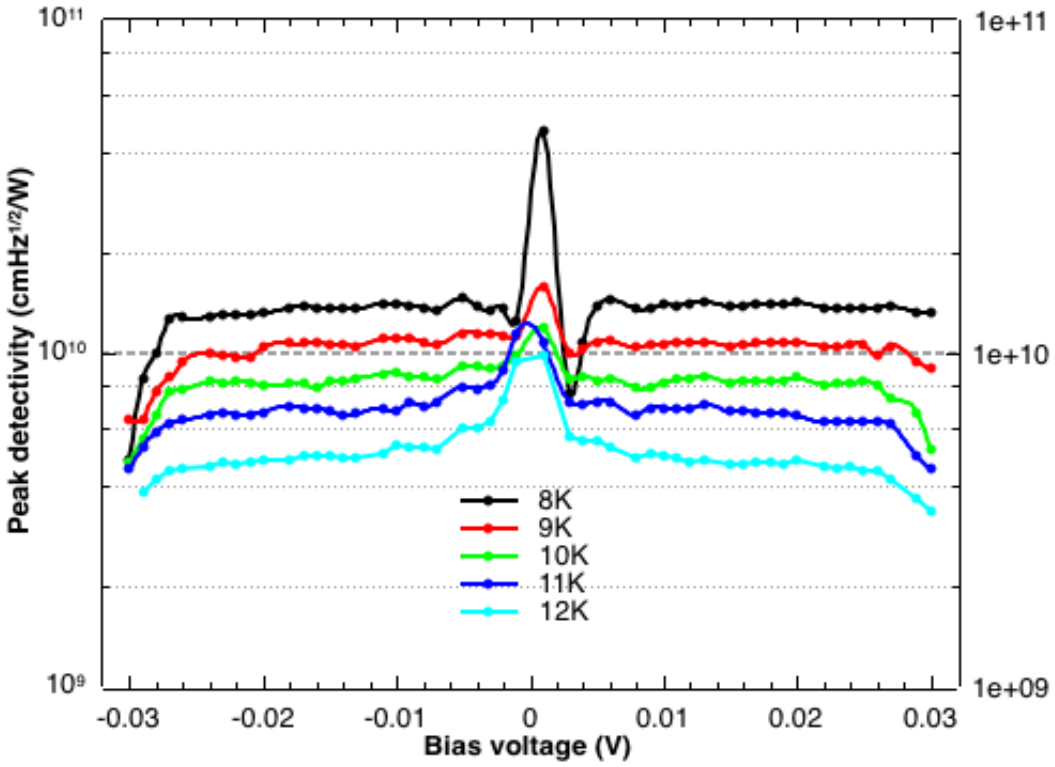

Figure 2.29 Calculated detectivity of G0219 (device size: 600 μm) from 9 K to 12 K

As shown in Figure 2.29, detectivity gradually decreases with both temperature and bias voltage. Peak detectivity, 4.63×10^{10} $cmHz^{1/2}/W$, is achieved under 8 K with around 1 mV, which is comparable with other terahertz photodetectors. Detectivity value slightly drops as device temperature increases. Within working bias range, device detectivity remains at the same level, around 10^{10} $cmHz^{1/2}/W$.

2.5 Conclusion

This chapter reports the theory, simulation model, characterization process and result of THz QWP. Working devices haven successfully demonstrated by measuring its BLIP temperature, absorption spectrum and responsivity. This device manages to reach a broadband absorption from 2.83 THz to 4.25 THz, with a peak absorption at 3.22 THz. Calibrated peak responsivity falls in the range of 0-2 A/W, reaching the highest peak responsivity of 1.9 A/W at 11 K under 26 mV. Its peak detectivity reaches up to 4.63×10^{10} $cmHz^{1/2}/W$. Furthermore, a reliable simulation model of THz QWIP is constructed, especially targeting at devices with absorption frequency around 3 THz.

In the future, more characterization can be done for THz QWP. To measure the absorption spectrum, more strict experiment condition is necessary to minimize the environment noise and device dark current. In ideal case, device needs to be cooled down to around 4 K in order to measure a clear and stable absorption spectrum. RF (radio frequency) characteristics can test device performance detecting fast signal. In general, QWIP and THz QWP involves photon interaction and can respond fast, with detecting frequency up to GHz range. More applications integrating THz QCL and THz QWP together, such as imaging and spectroscopy, will also be valuable for further research.

Chapter 3 Light Couplers for THz QWP

Due to the absorption selection rule of intersubband transition, light coupling strategy is always considered in the QWIP or THz QWP design. The prototype of light coupler is a 45° facet on a device substrate. Impinging light penetrates perpendicularly through the facet and bounces inside the substrate and the active region. However, it is important to realize normal incidence for photodetectors so that it can be implemented in focal plane array application. One of the typical light coupler for QWIP or THz QWP is metal grating coupler. Recently, there have been different light coupling strategy developed. This chapter demonstrate the mechanism and a theoretical model of the traditional 1D metal grating coupler and one of the cutting-edge coupling strategy, patch antenna coupler.

3.1 Metal Grating Coupler

Metal grating has been implemented in QWIP for a long history. The geometry of grating coupler can be specifically designed for different application. In QWIP, the most common

geometry of metal grating is 1D and 2D grating with rectangle or square shape. Integration with random grating has also been investigated [58]. Such coupling strategy improves the efficiency of QWIP device and has been implemented for a long time. This section introduces the mechanism and key parameters of metal grating coupler and presents the numerical solution for determining its optimal geometry using COMSOL.

3.1.1 Metal Grating Coupler Structure and Mechanism

Metal grating coupler is a typical light coupling strategy in QWIP and THz QWP. It can be easily fabricated and integrated with traditional device. By including metal grating coupler, normal incidence is realized; thus, this technique is widely implemented in QWIP or THz QWP FPAs.

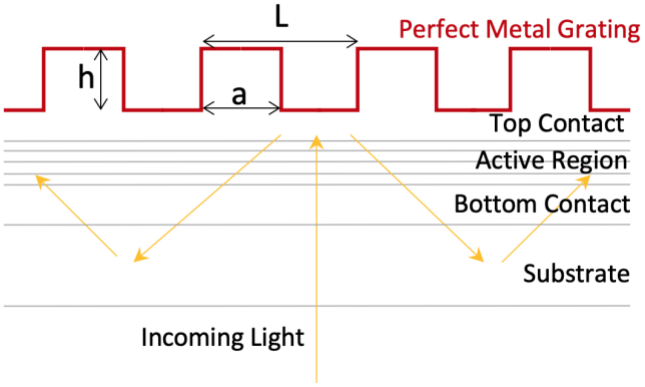

Figure 3.1 Schematic of metal grating coupler in QWIP, L: grating period, h: grating height and F: filling factor

Figure 3.1 illustrates the structure and mechanism of metal grating coupler, in which L is grating period, h is grating height and a represents the length that is not etched off to form diffraction grating structure. Metal grating layer fully covers the etched top contact of the device. Light

comes from back surface of the substrates but will not be absorbed when first time penetrating through active region. Incoming light is then diffracted by the grating structure, by which its polarization is rotated. Therefore, diffracted light can be absorbed, and intersubband selection rule is overcame.

3.1.2 Metal Grating Coupler Key parameters

In 1D metal grating coupler, there is a general rule to follow. To design a metal grating coupler in QWIP or THz QWP, grating period(L), grating height(h) and filling factor(F, $F = a/L$) are usually considered to optimize coupling performance. As a thumb of rule, grating period is chosen to be approximately the resonant wavelength inside the dielectric. In this case, diffraction angle can be maximized and high absorption can be achieved.

$$L = \frac{\lambda}{n_r} \tag{3.1}$$

where λ is resonant wavelength and n_r is refractive index of the dielectric material.
In general, grating height is set to be around one fourth of the inside wavelength and filling factor should be about 50%. These conditions will make the most of destructive interference and mostly eliminate zero-order diffraction.

To evaluate the performance of metal grating coupler in THz QWP, its coupling efficiency is defined based on the electric field distribution along growth direction in active region:

$$\eta = \left|E_y\right|^2 / |E|^2 \tag{3.2}$$

3.1.3 Simulation Results

Simulation model is constructed by commercial software COMSOL. 1D grating coupler structure for typical QWIP is simulated and compared with general designing rule to validate its reliability. In the COMSOL model, effect of dopants and multilayer structure are ignored for simplicity.

Since the intersubband transition only takes place given the optical electric field has a component along the growth direction, only TM mode will give rise to light absorption in quantum wells. Based on this assumption, COMSOL has been optimized by maximizing the average coupling efficiency inside the active region area. Figure 3.2 illustrates the geometries that is used to simulate QWIP device structure.

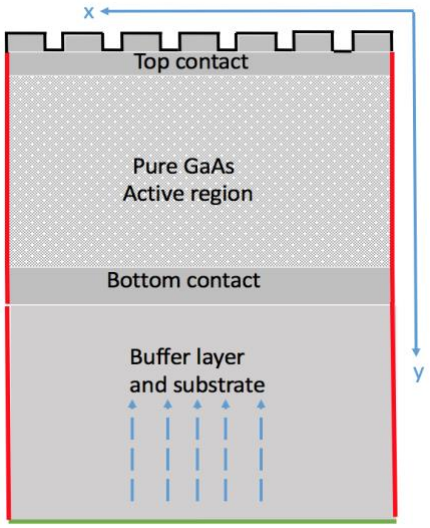

Figure 3.2 Schematic of numerical model geometry, light comes from the bottom side of substrate and is reflected and diffracted by metal grating structure on the top contact

By carefully designing the model geometry, boundary condition and port property, this model managed to generate meaningful coupling efficiency spectrum and optimize the peak efficiency around the wavelength of 5 μm. The electric field patterns at different wavelength are shown in Figure 3.3 as a justification. The thickness of both top and bottom contact layers are set to be 1 μm, and total active region is 5 μm thick. The substrate thickness is set to be only 10 μm to save the calculation time since it will not affect the coupling efficiency inside active region. Detail settings of the COMSOL model are included in Table 3.1.

As the figure presents, the electromagnetic field generated by the light inside dielectric clearly demonstrates the diffraction phenomenon, which changes dramatically in terms of the wavelength of light. Optimal diffraction is achieved in Figure 3.3(b), in which case the vertical component of electric field is maximized. It also shows that diffraction still can exist for lower wavelength, while diffracted beam can totally vanish as wavelength becomes higher than resonant wavelength inside the dielectric, in this case, GaAs.

Settings	Model dimension	Geometry	Boundary conditions			Refractive index
			Top	Sidewalls	Bottom	
Values	2D	22 μm × 17 μm	Perfect metal layer	Scattering boundary condition	Port	3.67

Table 3.1 Detail settings of the COMSOL model

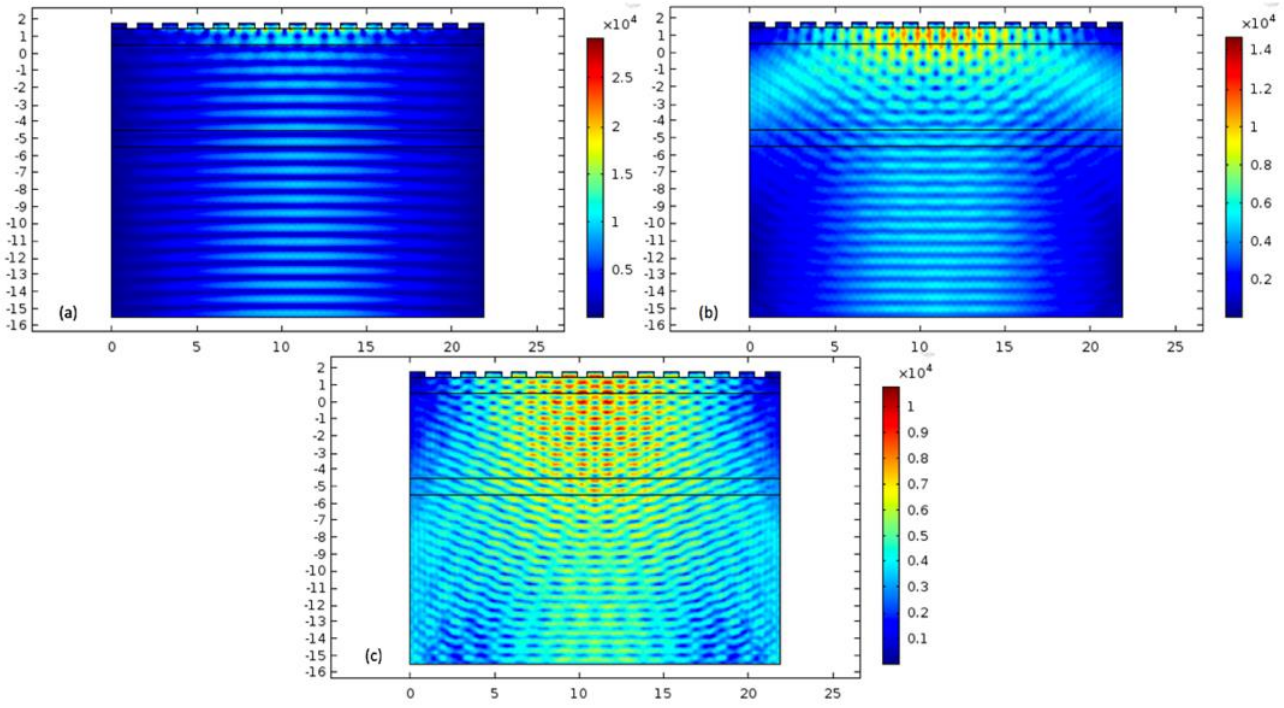

Figure 3.3 Simulation result on electric field pattern at different wavelength: (a) 6 µm, (b) 5 µm, and (c) 3.75 µm (L = 1.5 µm, h = 0.3 µm, F = 60%). x, y axes are in µm

To optimized coupling at resonant wavelength, grating period, height and filling factor are tuned to generate a series of efficiency spectrum.

Simulated result, as demonstrated in Figure 3.4, shows that the peak position of coupling efficiency spectrum shifts accordingly with the grating period.

The peak wavelength is around the inside wavelength in device material. Grating height and filling factor also play important roles in determining the peak value of coupling efficiency. It is shown that the coupling efficiency would stay optimal when the grating height is close to 20% of grating period, or with filling factor to be about 60% - 70%. Electric field distribution pattern at different wavelength clearly indicates the diffraction as the result grating structure.

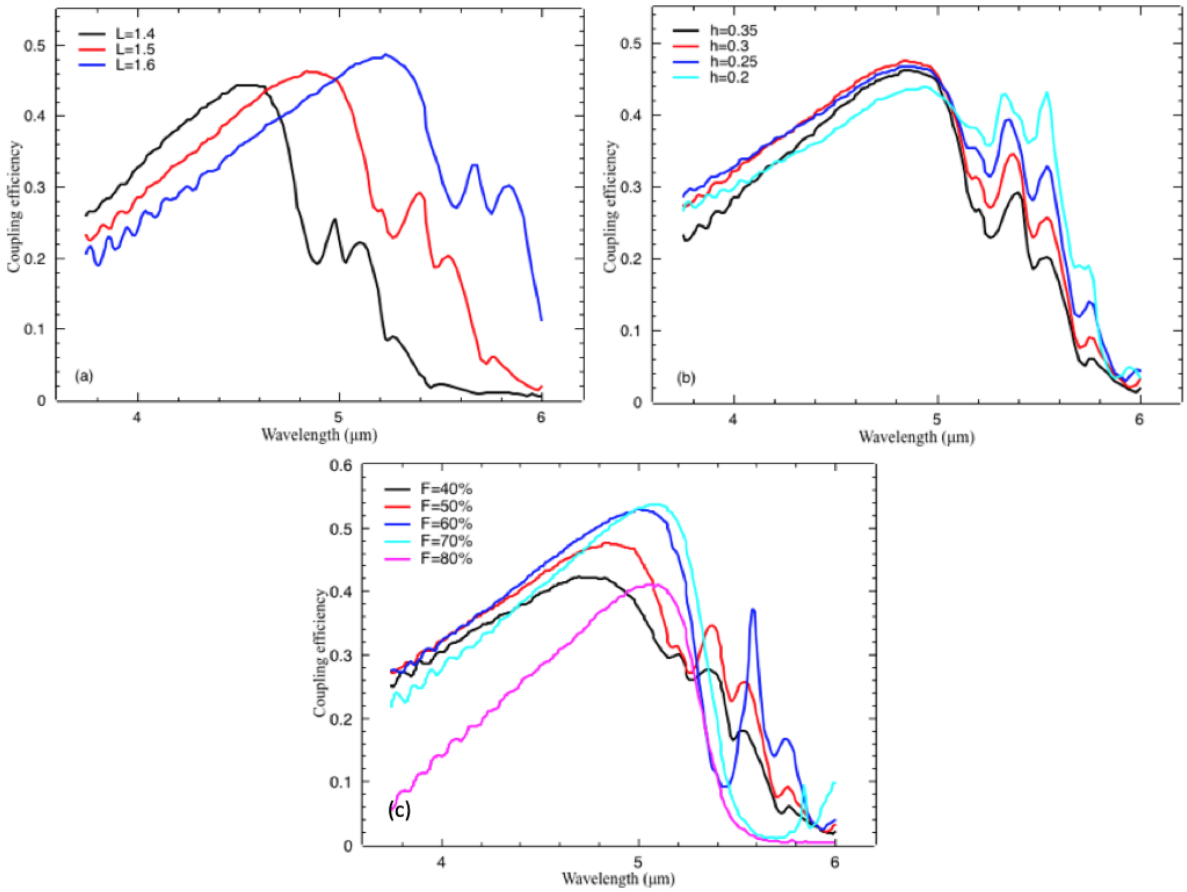

Figure 3.4 Simulation results of coupling efficiency with different (a) period (L), (b) height (h) and (c) filling factor (F)

As a result, to achieve highest coupling efficiency at 5μm, 1D grating structure with period to be 1.5 μm, grating height to be 0.3 μm and filling factor to be 60% is selected. By applying this metal grating structure, we can achieve peak coupling efficiency around 0.53.

According to the spectrum, the coupling efficiency shows a cut-off behavior at wavelength around 5 μm, which agrees with the diffraction mechanism. The relation between period length and cut-off wavelength is clearly demonstrated in Figure 3.4.

The additional peak which shown in Figure 3.4, when wavelength is higher than cut-off wavelength, varies a lot with grating height and filling factor, but stays exactly the same with grating period. From the view point of parameter designing, the grating height and filling factor are engineered to eliminate destructive interference. Therefore, the additional peak may come from the interference of the grating structure.

In conclusion, simulated results show a good agreement with general designing rule for 1D metal grating coupler in typical QWIP. This EM field simulation model is convincing and will be further applied in the following patch antenna simulation.

3.2 Patch Antenna

Application of antenna structure in QWIP devices has been recently investigated; a few papers reported promising results [37], [39], [40] in boosting QWIP and THz QWP temperature performance compared with conventional geometries. Patch antenna not only traps surrounding normal-incident light inside the microcavities by its antenna effect, but also reduces the surface area of the device as well as its dark currents; thus, device performance gets boosted and its detectivity increases.

Very low frequency THz QWP, owing to low aluminum fraction in quantum barrier regions, is mainly limited by its poor temperature performance. Integrating antenna structures in very low

frequency THz QWP can become a potential solution to widen the range of its applications. In this thesis, simulation of patch antenna structure in THz QWP is investigated.

3.2.1 Patch Antenna Mechanism

Patch antenna is a light coupling geometry that utilize double metal layers as a resonant absorber. Light at resonant frequency is then absorbed and confined at semiconductor slab between metal layers. Therefore, to integrate patch antenna on THz QWP, device active region will be etched down to form a mesa array, in which mesa size, height and distance between adjacent mesas need to be carefully designed to match designed intersubband transition.

Figure 3.5 presents a square-shape patch antenna structure.

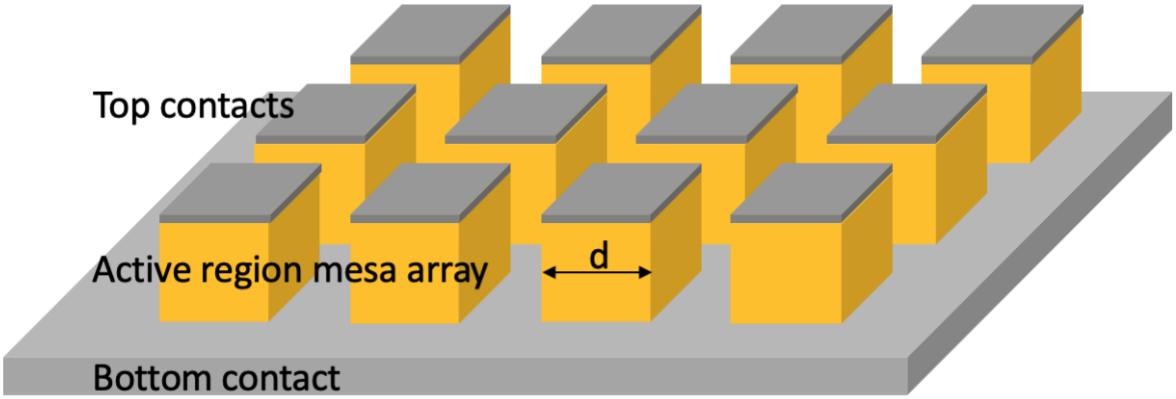

Figure 3.5 Schematic of patch antenna structure in QWIP, d is the size of waveguide cavity

Compared to conventional 45° geometry, double-metal patch antenna improves light coupling by expanding actual light collecting area. Meanwhile, device dark current is reduced as total size of

mesa array is smaller than regular large mesa. As a result, given by (2.32), detectivity at high temperature regime (dark current limited regime) is further boosted.

3.2.2 Patch Antenna THz QWP Key parameters

In a Fabry-Perot resonator, like double-metal patch antenna, standing wave pattern can be written as

$$\nu_k = \frac{cK}{2n_{eff}d} \tag{3.3}$$

where c is the speed of light, K is the mode number in the electromagnetic(EM) field, n_{eff} is effective refractive index inside the dielectric and d is the size of waveguide cavity.

For a patch antenna array, reflectivity can be experimentally measured and will show absorption valley at resonant frequency in spectrum. The reflectivity can be expressed in Lorentzian approximation [59] as

$$R(\nu) = 1 - \frac{C}{1 + \frac{(\nu - \nu_0)^2}{\pi^2 \nu_0^2} Q^2} \tag{3.4}$$

where $R(\nu)$ is spectral reflectivity at frequency ν, ν_0 is resonant frequency which, in this case, is ν_k when $K = 1$. In this equation, there are two new figures of merit that can be extracted, C and Q. C is called contrast and Q is defined as quality factor of patch antenna. Given reflectivity spectrum [59],

$$C = 1 - R_{min} \tag{3.5}$$

where R_{min} is the minimum spectral reflectivity at resonant frequency and $\Delta\upsilon$ is the full width at half maximum(FWHM) of reflectivity valley.

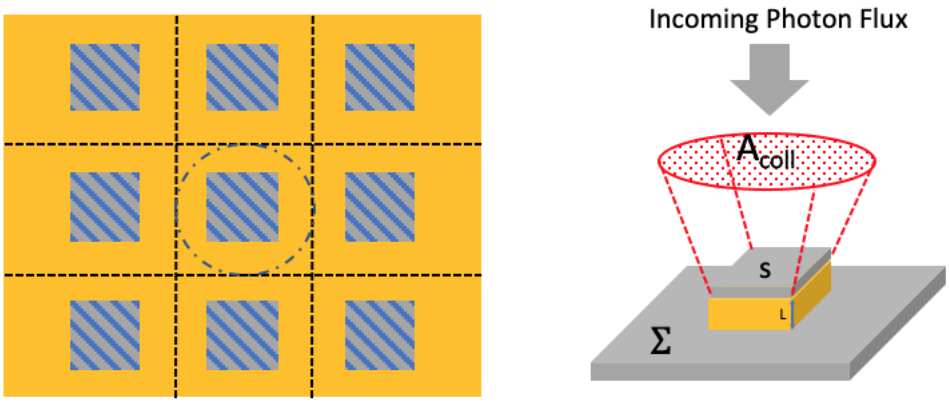

Figure 3.6 Top view of patch antenna structure and schematic of how patch antenna works [39]

Figure 3.6 shows a schematic representation of patch antenna structure with its key parameters. As it illustrates, for each mesa in one unit cell with area of $\sum$, photon flux vertically shines to the top contact surface; and photons inside its collection area A_{coll} can be coupled and then absorbed. Given collection area A_{coll} and photon flux ϕ, total number of photons absorbed by the detector per unit time can be represented as $A_{coll}\phi$.

A_{coll} can be calculated by

$$A_{coll} = C\Sigma \tag{3.7}$$

Therefore, to maximize antenna effect, contrast C needs to be optimized.

To evaluate the improvement on device temperature performance when including patch antenna structure, some models have already been developed. According to D. Palaferri [39], the internal responsivity of the structure, *R*, can be represented as

$$R = B_{isb} Q \frac{eg}{N_{qw} E_{21}} \tag{3.8}$$

where Q is quality factor of the structure; B_{isb} describes the portion EM field been absorbed by quantum transition. B_{isb} can be further expressed as a function of incident photon energy, which is [39]

$$B_{isb}(E) = \frac{N_{qw} L_{qw}}{L} \frac{E_p^2}{4E_{21}} \frac{\hbar\Gamma}{(E - E_{21})^2 + \frac{(\hbar\Gamma)^2}{4}} = \eta(E) \frac{\cos\theta}{\sin^2\theta} \frac{\lambda_{21}}{2\pi L} \tag{3.9}$$

where N_{qw} is total number of quantum wells between double metal layers, L_{qw} is the width of a quantum well, L is the total thickness inside double metal structure, E_{21} is the energy gap between ground state and first excited state, E_p is plasma frequency that determined by the total number of free carriers that are available for photon absorption, $\hbar\Gamma$ is the linewidth of quantum transition, $\eta(E)$ is the absorption strength that given by (2.9), incident angle $\theta = 45°$ for conventional THz QWP geometry and resonant frequency $\lambda_{21} = hc/E_{21}$.

Assuming, in conventional THz QWP, $A_{coll} = S$. The relation between BLIP temperature for traditional mesa device, T_{blip}^0, and for patch antenna device, T_{blip}, can be written as [39]

$$T_{blip} = \frac{T_{blip}^0}{1 - \frac{k_b T_{blip}^0}{E_{21}} \left[lnF - lnK + ln\left(\frac{T_{blip}^0}{T_{blip}}\right) \right]} \tag{3.10}$$

where F and K are defined as [39]

$$F = \frac{A_{coll} \lambda_{21} Q}{V} \tag{3.11}$$

$$K = \frac{2\pi \cos\theta}{\sin^2\theta} t \tag{3.12}$$

where $V = SL$ is the volume of patch antenna cavity and t is the transmission coefficient of the semiconductor facet.

3.2.3 Simulation Results

Numerical simulation is constructed using COMSOL with similar setup as the previous section. Moreover, a 3D numerical model is built to solve the electric distribution inside active region and the reflectance of patch antenna array. The goal of numerical simulation is to compare the simulated results with published data to validate the COMSOL model.

This 10-by-10 patch antenna array is composed of three layers, bottom and top contact metal layers and active region layer. The material selected for active region is pure GaAs, where the aluminum doping is ignored for simplicity. The size of each patch antenna is determined by (3.3). Incoming light shines from a port above top contact surface and penetrate through air layer before reaching to patch antenna array. After coupled by patch antenna structure, light with certain wavelength can be confined with in all the square mesas and sustain within active region. Figure 3.7 shows an example of electric pattern inside the active region layer. The diagonal distribution comes from the initialization of impinging light in the software. It clearly reveals the light confinement by patch antenna array and shows high uniformity across the whole surface area.

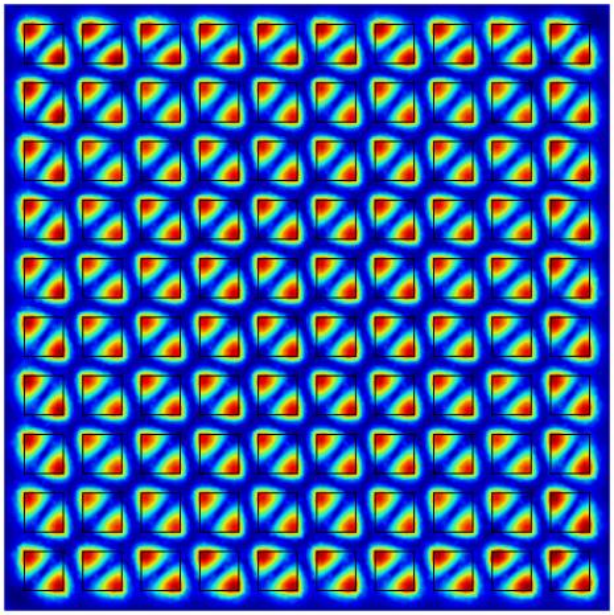

Figure 3.7 Electric field distribution pattern of patch antenna coupling structure

Reflectivity of patch antenna structure is also simulated and compared with published result. Demo patch antenna structure is extracted from [39], with a mesa size of 10 μm and mesa height of 2 μm. Period length is set to be 15 μm which reaches the lowest reflectivity according to the experiment result from the reference. Real refractive index of GaAs is set to be 3.5 in the COMSOL model.

Figure 3.8 presents the comparison between simulation result and experiment data extracted from reference. As it shows, the simulation follows the experiment results closely, with the same minimum reflectivity value of 10%. Simulated peak reflectivity frequency is around 4.45 THz, which is slight red shifted compared with extracted data. This difference may be caused by ambiguous permittivity of GaAs material.

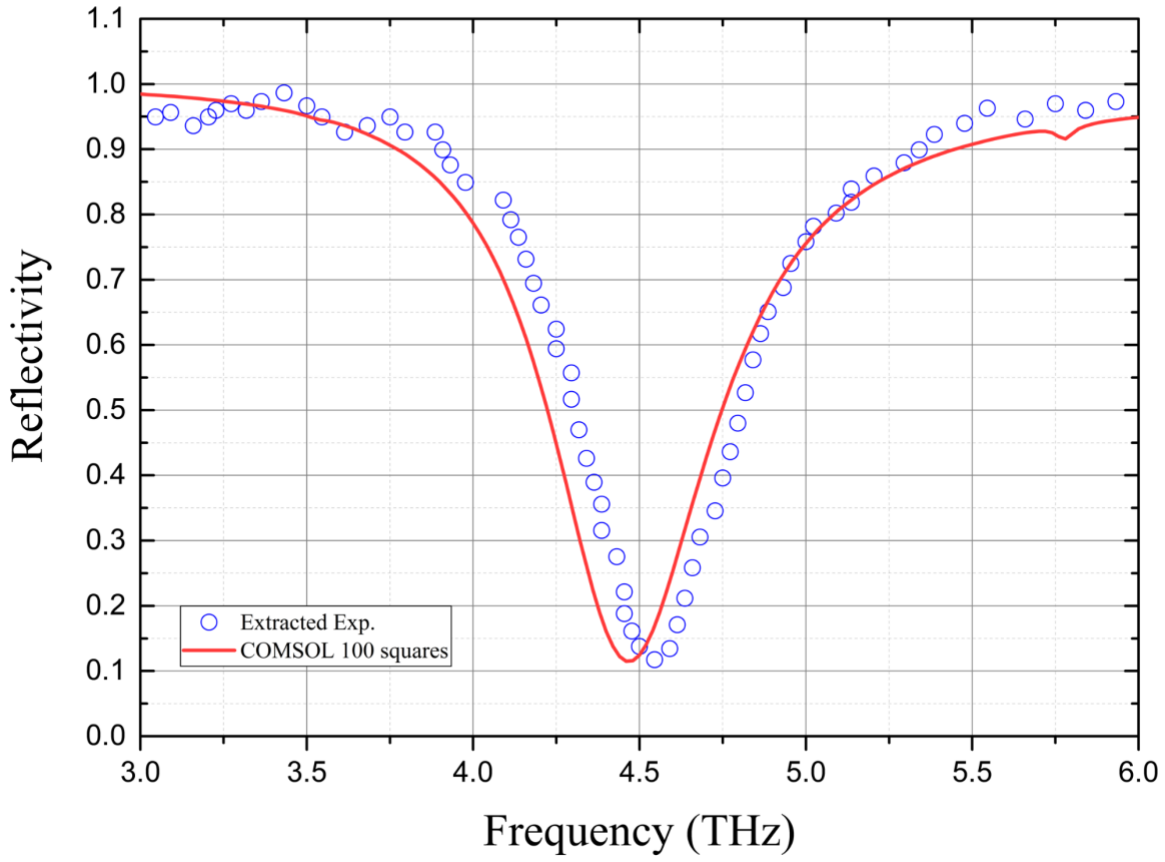

Figure 3.8 Calculated reflection of patch antenna structure compared with measurement result from [39]

In conclusion, the numerical simulation model has been developed and compared with published data. Electric field patterns are displayed and the physical meaning behind them is well analyzed. Furthermore, the absorption of patch antenna structure is calculated, which aligns with published data. These validation results prove the reliability of numerical model, which, along with theoretical basis, can be applied into designing and analyzing different light coupling structures for QWIP and THz QWP devices.

3.3 Conclusion

This chapter presents the theoretical model and numerical solutions of both traditional metal grating coupler and novel patch antenna structure. It provides fundamental basis for designing and analysis THz QWP with more antenna structure. Besides these two light coupling strategies, there are other coupling methods that targeting at different wavelength with different application. One of the future research interest is to improve the QWIP or THz QWP performance in RF fields. QWIP and THz QWP is mostly featured as their fast response, which has more potential in applications such as detecting beat notes. QWIPs with GHz-range detection speed has been realized by integrating air-bridge structure and microstrip antenna [60].

Chapter 4 Conclusion and Future Work

This thesis reports a comprehensive study on the development of THz QWP. MATLAB simulation model is constructed to simulate THz QWP active region and absorption spectrum. THz QWP is grew, fabricated and further tested. Measurement results are included which demonstrates its working performance. Simulation model based on COMSOL is built to investigate different light coupling structures in THz QWP.

Working principles of THz QWP are first introduced. Active region design is discussed together with many body effects which played an important role in designing THz QWP. Figures of merit in THz QWP, including dark current, responsivity and detectivity, are presented. Simulation model using MATLAB is built and compared with published measurement results in literatures.

A new THz QWP design targeting at 3 THz is proposed and fabricated for testing. Experiment setups are reported in this thesis, together with a comprehensive discussion on measurement results, including device dark current, background current, photocurrent and absorption spectrum. Furthermore, parameters like BLIP temperature, responsivity and detectivity are analyzed to demonstrate device performance. Besides, the difference in dark current density

among devices with different mesa sizes is also discussed, which is potentially attributed to sidewall leakage current. Sidewall passivation process is expected to eliminate leakage current and improve device performance. In conclusion, this THz QWP with new active region design has its BLIP temperature at 10 K and manages to achieve terahertz range absorption at lower frequency around 3 THz. According to measurement results, it achieves highest absorption responsivity around 1.9 A/W at 11 K under bias voltage of 26 mV and highest detectivity of 4.63×10^{10} $cmHz^{1/2}/W$ at 8 K under 1 mV. Measured absorption peak is located at 107.32 cm^{-1} (3.22 THz) with an absorption broadening around 1.42 THz at 7.7 K under 25 mV.

In the last chapter, COMSOL numerical model on different light coupling structures are presented. 1D metal grating and patch antenna structure are investigated and their numerical solutions are compared with published data. Simulated electric field patterns are displayed and analyzed. Moreover, the reflection of patch antenna structure is calculated, which agrees with published measurement data in the literature. These validation results prove the reliability of numerical model, which, along with theoretical basis, can be applied into designing and implementing light coupling structures for THz QWP devices.

Overall, a comprehensive study of THz QWP, including theoretical principles, simulation model, experiment setup and analysis on testing results, is reported in this thesis. Numerical solutions on light coupling structure are presented as well and can be further implemented in THz QWP in future research. THz QWP working at 3 THz is challenging to be achieved because of the high requirements in MBE growth and characterization systems. Fabricated THz QWP (G0219) manages to realize low frequency absorption near 3THz, and will have strong potentials in either

further improving its performance by implementing light coupling structures or combining with THz QCL at similar emission wavelength for applications in spectroscopy and wireless communications.

Based on current achievements in developing THz QWP at 3 THz, there are three directions that can be distinguished to work on in the future.

First, THz QWP can be combined with different light couplers. For instances, patch antenna structure in QWIP has been demonstrated, which improves QWIP performance in high temperature regime. QWIP with air-bridge structure and microstrip have achieved high-speed response up to 26 GHz and beatnote detection. These coupling techniques have not been fully developed in THz QWP, therefore need to be further investigated for their implementation with THz QWP.

Second, there are many researches can be carried out for designing the applications using THz QWP. By fabricating metal grating coupler, FPA of THz QWPs can be achieved for imaging application. Moreover, by combining THz QWP with THz QCL using wafer transfer, it is possible for ultrafast spectroscopy in terahertz frequency using single device. In addition, it is also interesting for realizing terahertz communication using THz QWP and QCL or other THz sources.

Finally, active region design of THz QWP still has lots of room to be improved. At present, THz QWP is based on single-well design and suffers from high dark current caused by thermal

activation. Quantum cascade detectors in terahertz region has been proposed but not further developed for years. Designing strategies from THz QCL can be introduced in designing more complicated active region for THz QWP, which may reduce detector dark current and increase its absorption strength. As mentioned, many body effects can significantly change the actual quantum well structure and shift absorption peak. There are other phenomena, such as dopant segregation and nonlinear electric field distribution along active region, will also affect detector performance, that are short of development in THz QWP model.

References

[1] B. F. Levine, "Quantum-well infrared photodetectors," *J. Appl. Phys. J. Appl. Phys. Phys. Lett. Phys. Lett. Appl. Phys. Lett. J. Appl. Phys*, vol. 74, no. 73, pp. 1–641, 1993.

[2] J. C. Chiang, S. S. Li, and A. Singh, "A two-stack indirect-barrier/triple-coupled quantum well infrared detector for mid-wavelength and long-wavelength infrared dual band detection," *Appl. Phys. Lett.*, vol. 71, no. 24, pp. 3546–3548, 1997.

[3] M. Z. Tidrow, X. Jiang, S. S. Li, and K. Bacher, "A four-color quantum well infrared photodetector," *Appl. Phys. Lett.*, vol. 74, no. 9, pp. 1335–1337, 1999.

[4] H. C. Liu, C. Y. Song, A. J. SpringThorpe, and J. C. Cao, "Terahertz quantum-well photodetector," *Appl. Phys. Lett.*, vol. 84, no. 20, pp. 4068–4070, May 2004.

[5] H. Li *et al.*, "6.2-GHz modulated terahertz light detection using fast terahertz quantum well photodetectors," *Sci. Rep.*, vol. 7, no. 1, pp. 1–12, 2017.

[6] J. B. Baxter and G. W. Guglietta, "Terahertz Spectroscopy," *Anal. Chem.*, vol. 83, no. 12, pp. 4342–4368, Jun. 2011.

[7] G. Folpini, K. Reimann, M. Woerner, T. Elsaesser, J. Hoja, and A. Tkatchenko, "Strong Local-Field Enhancement of the Nonlinear Soft-Mode Response in a Molecular Crystal," *Phys. Rev. Lett.*, vol. 119, no. 9, p. 097404, Sep. 2017.

[8] M. Krüger, S. Funkner, E. Bründermann, and M. Havenith, "Uncertainty and Ambiguity in Terahertz Parameter Extraction and Data Analysis."

[9] M. Tonouchi, “Cutting-edge terahertz technology,” *Nat. Photonics*, vol. 1, no. 2, pp. 97–105, 2007.

[10] Y. Oyama, L. Zhen, T. Tanabe, and M. Kagaya, “Sub-terahertz imaging of defects in building blocks,” *NDT E Int.*, vol. 42, no. 1, pp. 28–33, Jan. 2009.

[11] M. Dohi *et al.*, “Application of terahertz pulse imaging as PAT tool for non-destructive evaluation of film-coated tablets under different manufacturing conditions,” *J. Pharm. Biomed. Anal.*, vol. 119, pp. 104–113, Feb. 2016.

[12] F. Sizov, “THz radiation sensors,” *Opto-Electronics Rev.*, vol. 18, no. 1, p. 10, Jan. 2010.

[13] F. Sizov and A. Rogalski, “THz detectors,” *Prog. Quantum Electron.*, vol. 34, no. 5, pp. 278–347, Sep. 2010.

[14] M. Fujiwara and N. Hiromoto, “Ge:Ga Far-infrared Photoconductor with a Low Ga Concentration of $\mathbf{1\times10^{14}\ cm^{-3}}$,” *Jpn. J. Appl. Phys.*, vol. 36, no. Part 1, No. 7A, pp. 4262–4266, Jul. 1997.

[15] W. J. Moore and H. Shenker, “A high-detectivity gallium-doped germanium detector for the 40–120μ region,” *Infrared Phys.*, vol. 5, no. 3, pp. 99–106, Sep. 1965.

[16] N. M. Haegel, E. E. Haller, and P. N. Luke, “Performance and materials aspects of Ge:Be photoconductors,” *Int. J. Infrared Millimeter Waves*, vol. 4, no. 6, pp. 945–954, Nov. 1983.

[17] J. R. Sandercock, “Energy exchange between hot carriers and the lattice in indium antimonide,” *Proc. Phys. Soc.*, vol. 86, no. 6, pp. 1221–1224, Dec. 1965.

[18] G. E. Stillman, C. M. Wolfe, and J. O. Dimmock, “Chapter 4 Far-Infrared Photoconductivity in High Purity GaAs,” *Semicond. Semimetals*, vol. 12, pp. 169–290, Jan. 1977.

[19] L. C. Lenchyshyn, H. C. Liu, M. Buchanan, and Z. R. Wasilewski, "An asymmetric quantum well infrared photodetector with voltage-tunable narrow and broad-band response," *J. Appl. Phys.*, vol. 79, no. 6, pp. 3307–3311, 1996.

[20] H. Schneider, C. Schönbein, M. Walther, K. Schwarz, J. Fleissner, and P. Koidl, "Photovoltaic quantum well infrared photodetectors: The four-zone scheme," *Appl. Phys. Lett.*, vol. 71, no. 2, pp. 246–248, 1997.

[21] R. Rehm *et al.*, "Bispectral thermal imaging with quantum-well infrared photodetectors and InAs/GaSb type-II superlattices," *Proc. SPIE*, vol. 6206, p. 62060Y–62060Y–11, 2006.

[22] L. Gendron, M. Carras, A. Huynh, V. Ortiz, C. Koeniguer, and V. Berger, "Quantum cascade photodetector," *Appl. Phys. Lett.*, vol. 85, no. 14, pp. 2824–2826, 2004.

[23] F. R. Giorgetta *et al.*, "Quantum cascade detectors," *IEEE J. Quantum Electron.*, vol. 45, no. 8, pp. 1039–1052, 2009.

[24] J. H. Lee, S. S. Li, M. Z. Tidrow, W. K. Liu, and K. Bacher, "Quantum-well infrared photodetectors with digital graded superlattice barrier for long-wavelength and broadband detection," *Appl. Phys. Lett.*, vol. 75, no. 20, pp. 3207–3209, 1999.

[25] A. V Barve *et al.*, "High temperature operation of quantum dots-in-a-well infrared photodetectors," *Infrared Phys. Technol.*, vol. 54, no. 3, pp. 215–219, 2011.

[26] M. Graf *et al.*, "Terahertz range quantum well infrared photodetector," *Appl. Phys. Lett.*, vol. 84, no. 4, pp. 475–477, Jan. 2004.

[27] J. C. Cao and H. C. Liu, "Chapter 4 - Terahertz Semiconductor Quantum Well Photodetectors," *Semicond. Semimetals*, vol. 84, pp. 195–242, 2011.

[28] X. G. Guo, J. C. Cao, R. Zhang, Z. Y. Tan, and H. C. Liu, "Recent progress in terahertz

quantum-well photodetectors," *IEEE J. Sel. Top. Quantum Electron.*, vol. 19, no. 1, 2013.

[29] P. D. Grant, S. R. Laframboise, R. Dudek, M. Graf, A. Bezinger, and H. C. Liu, "Terahertz free space communications demonstration with quantum cascade laser and quantum well photodetector," *Electron. Lett.*, vol. 45, no. 18, p. 952, 2009.

[30] Z. Chen *et al.*, "Wireless communication demonstration at 4.1 THz using quantum cascade laser and quantum well photodetector," *Electron. Lett.*, vol. 47, no. 17, p. 1002, 2011.

[31] T. Zhou *et al.*, "Terahertz imaging with quantum-well photodetectors," *IEEE Photonics Technol. Lett.*, vol. 24, no. 13, pp. 1109–1111, 2012.

[32] T. Zhou, R. Zhang, X.-G. Guo, Z.-Y. Tan, and J.-C. Cao, "THz Imaging Using a Quantum-Well Photodetector with Background Limited Performance," *Chinese Phys. Lett.*, vol. 29, no. 10, p. 104202, Oct. 2012.

[33] F. Wu *et al.*, "Terahertz intersubband transition in GaN/AlGaN step quantum well," *J. Appl. Phys.*, vol. 113, no. 15, p. 154505, Apr. 2013.

[34] D. Feezell, Y. Sharma, and S. Krishna, "Optical properties of nonpolar III-nitrides for intersubband photodetectors," *J. Appl. Phys.*, vol. 113, no. 13, p. 133103, Apr. 2013.

[35] R. Zhang *et al.*, "Terahertz Quantum Well Photodetectors With Metal-Grating Couplers," *IEEE J. Sel. Top. Quantum Electron.*, vol. 23, no. 4, pp. 1–7, Jul. 2017.

[36] and J. C. C. R. Z. D. X. S. Z. L. F. H. X. W. T. Z. Z. Y. Tan, "Terahertz Quantum Well Photodetectors with Metal-Grating Couplers," *IEEE J. Sel. Top. Quantum Electron.*, vol. 23, no. 4, 2017.

[37] D. Palaferri *et al.*, "Patch antenna terahertz photodetectors," *Appl. Phys. Lett.*, vol. 106, no. 16, p. 161102, Apr. 2015.

[38] B. Paulillo, J.-M. Manceau, L. H. Li, A. G. Davies, E. H. Linfield, and R. Colombelli, "Room temperature strong light-matter coupling in three dimensional terahertz meta-atoms," *Appl. Phys. Lett.*, vol. 108, no. 10, p. 101101, Mar. 2016.

[39] D. Palaferri, Y. Todorov, A. Mottaghizadeh, G. Frucci, G. Biasiol, and C. Sirtori, "Ultra-subwavelength resonators for high temperature high performance quantum detectors," *New J. Phys.*, vol. 18, no. 11, p. 113016, Nov. 2016.

[40] D. Palaferri *et al.*, "Room-temperature nine-µm-wavelength photodetectors and GHz-frequency heterodyne receivers," *Nature*, vol. 556, no. 7699, pp. 85–88, Mar. 2018.

[41] H. C. Liu, H. Luo, C. Song, Z. R. Wasilewski, A. J. Springthorpe, and J. C. Cao, "Terahertz Quantum Well Photodetectors," vol. 14, no. 2, pp. 374–377, 2008.

[42] H. (Harald) Schneider and H. C. Liu, *Quantum well infrared photodetectors : physics and applications*. Springer, 2007.

[43] E. Rosencher and B. Vinter, *Optoelectronics*. Cambridge University Press, 2002.

[44] M. Graf *et al.*, "Terahertz quantum well infrared detectors," *Infrared Phys. Technol.*, vol. 52, no. 6, pp. 289–293, Nov. 2009.

[45] S. Ferré, S. G. Razavipour, and D. Ban, "Terahertz quantum well photodetectors with improved designs by exploiting many-body effects," *Appl. Phys. Lett.*, vol. 103, no. 8, p. 081105, Aug. 2013.

[46] W. L. Bloss and W. L., "Effects of Hartree, exchange, and correlation energy on intersubband transitions," *J. Appl. Phys.*, vol. 66, no. 8, pp. 3639–3642, Oct. 1989.

[47] L. Hedin, B. I. Lundqvist, and S. Lundqvist, "Local exchange-correlation potentials," *Solid State Commun.*, vol. 9, no. 9, pp. 537–541, 1971.

[48] S. D. Gunapala *et al.*, "High performance InGaAs/GaAs quantum well infrared

photodetectors," *Appl. Phys. Lett.*, vol. 64, no. 25, pp. 3431–3433, Jun. 1994.

[49] E. Rosencher, B. Vinter, F. Luc, L. Thibaudeau, P. Bois, and J. Nagle, "Emission and capture of electrons in multiquantum-well structures," *IEEE J. Quantum Electron.*, vol. 30, no. 12, pp. 2875–2888, 1994.

[50] Z. Y. Tan *et al.*, "Temperature dependence of current–voltage characteristics of terahertz quantum-well photodetectors," *Semicond. Sci. Technol.*, vol. 24, no. 11, p. 115014, Nov. 2009.

[51] A. Benz *et al.*, "Resonant metamaterial detectors based on THz quantum-cascade structures," *Sci. Rep.*, vol. 4, no. 1, p. 4269, May 2015.

[52] W. Wu, A. Bonakdar, and H. Mohseni, "Plasmonic enhanced quantum well infrared photodetector with high detectivity," *Appl. Phys. Lett.*, vol. 96, no. 16, p. 161107, Apr. 2010.

[53] S. Kalchmair *et al.*, "Detectivity enhancement in quantum well infrared photodetectors utilizing a photonic crystal slab resonator," *Opt. Express*, vol. 20, no. 5, p. 5622, Feb. 2012.

[54] H. C. Liu, H. Luo, C. Y. Song, Z. R. Wasilewski, A. J. S. Thorpe, and J. C. Cao, "Design of terahertz quantum well photodetectors," 2006.

[55] J. Y. Jia *et al.*, "Dark current mechanism of terahertz quantum-well photodetectors," *Cit. J. Appl. Phys.*, vol. 116, p. 194507, 2014.

[56] H. C. Liu, "Dependence of absorption spectrum and responsivity on the upper state position in quantum well intersubband photodetectors," *J. Appl. Phys.*, vol. 73, no. 6, pp. 3062–3067, Mar. 1993.

[57] A. Gomez, V. Berger, N. Péré-Laperne, and L.-A. De Vaulchier, "Barrier breakdown in

multiple quantum well structure," *Appl. Phys. Lett.*, vol. 92, no. 20, p. 202110, May 2008.

[58] B. Xing and H. C. Liu, "Simulation of one-dimensional quasi-random gratings for quantum well infrared photodetectors," *J. Appl. Phys.*, vol. 80, no. 2, pp. 1214–1218, 1996.

[59] C. Feuillet-Palma, Y. Todorov, A. Vasanelli, and C. Sirtori, "Strong near field enhancement in THz nano-antenna arrays," *Sci. Rep.*, vol. 3, no. 1, p. 1361, Dec. 2013.

[60] E. Rodriguez *et al.*, "Room-Temperature, Wide-Band, Quantum Well Infrared Photodetector for Microwave Optical Links at 4.9 μm Wavelength," *ACS Photonics*, vol. 5, no. 9, pp. 3689–3694, Sep. 2018.

Appendices

Appendix A Growth Sheet

THz QWP at 3 THz (G0219)

Total growth thickness: 39435 Å

Material	x	d(Å)	Doping(cm^{-3})	reps
GaAs		8000	1.00E+17	
$Al_xGa_{1-x}As$	0.015	951		×23
GaAs		28.5		
GaAs		100	4.00E+16	
GaAs		28.5		
$Al_xGa_{1-x}As$	0.015	951		
GaAs		4000	1.00E+17	

Table A.1 Growth layer structure of G0219

Appendix B Fabrication Process Sheet

No	Process Step	Detail
1	Wafer cleaving	Cleave wafer into an 1 cm×1 cm piece
2	Precleaning	Acetone wash with ultrasonic
		Isopropanol wash with ultrasonic
		DI water rinse
		Ni blow dry
3	Photoresist spin coating	Photoresist PMGI-SF7 spin coating
		Bake
		Photoresist S1811 spin coating
		Bake
4	Photolithography	Mask name: ‘Chao_THzQWP_mesatop_1’
		Dose: 120 mJ/cm2; wavelength: 415 nm
5	UV development	MF 319 dip
		DI water rinse
		Ni blow dry

6	Mesa metal deposition	O_2 plasma
		BOE dip
		DI water rinse
		Ni blow dry
		E-beam metal deposition: Ni/Ge/Au
		Metal liftoff
		Remove-PG dip
		Acetone wash
		Isopropanol wash
		DI water rinse
		Ni blow dry
7	Metal Annealing	
8	Mesa etch pattern spin coating	Photoresist AZP4620 spin coating
		Bake
9	Photolithography	Mask name: ‘Chao_THzQWP_mesaetch_2’
		Dose: 1000 mJ/cm^2; wavelength: 415 nm
10	UV development	AZ400K dip
		DI water rinse
		Ni blow dry

11	Mesa dry etching	ICP-RIE etching
12	Bottom metal contact spin coating	Photoresist PMGI-SF7 spin coating
		Bake
		Photoresist S1811 spin coating
		Bake
13	Photolithography	Mask name: ‘Chao_THzQWP_bottomcontact_3’
		Dose: 120 mJ/cm^2; wavelength: 415 nm
14	UV development	MF 319 dip
		DI water rinse
		Ni blow dry
15	Bottom metal deposition	O_2 plasma
		BOE dip
		DI water rinse
		Ni blow dry
		E-beam metal deposition: Ni/Ge/Au
		Metal liftoff
		Remove-PG dip
		Acetone wash

		Isopropanol wash
		DI water rinse
		Ni blow dry
16	Post cleaning	Remove-PG dip
		Acetone wash with ultrasonic
		Isopropanol wash with ultrasonic
		DI water rinse
		Ni blow dry
		O_2 plasma
17	Lapping	45° facet lapping

Table B.1 Fabrication processing sheet

Appendix C Device Packaging

Packaging process is divided into four steps: bar cleaving, 45° facet polishing, mounting and wire-bounding. Figure C.1 illustrates the four-step packaging process of THz QWP device. After fabrication and cleaning, the 2 cm×2 cm square wafer is then cleaved into three bars. Each bar contains a set of devices with different mesa length. After cleaving, each device bar can be processed separately to make three packages.

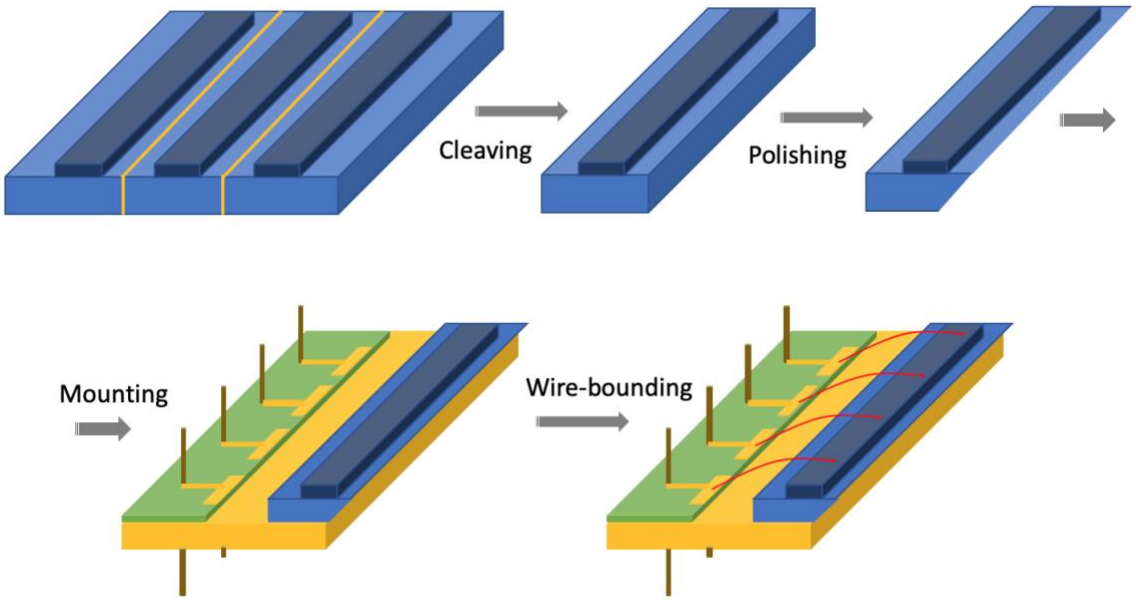

Figure C.1 Schematic of packaging process

At the edge of device side, the side surface of GaAs substrate is polished to a 45° facet. Device bar is first glued on the home-made aluminum holder with a 45° trench. Top surface with devices is fully covered with wax to avoid damage. Hand-polishing is then performed by pressing the holder with sample successfully onto sandpapers with 600 and 1200 grits. During polishing

process, sample holder is continuously rinsed by deionized water. After reaching an atom-flat facet, device bar is dismounted from the holder and dip in acetone solution to remove residual wax.

After polishing, device bar is mounted on a home-made package. This package is manufactured with oxygen-free copper and coated with gold by electroplating. It is specially designed so that the 45° facet can vertically face the impinging light. Device is mounted on the package by applying thin indium layer and warm it up to its melting point. Due to back-side gold layer, device bar can form an indium-gold bond with package to secure its position. A circuit board is glued on package by silver epoxy for wire-bounding. Finally, top and bottom contacts are connected with the circuit board by gold wire using ball bonding machine and the device is ready for testing.